Supplemental Information

Methods

Cloning, Expression, and Purification of MIP-1 and IDE:

The synthetic genes that encode mature form of human MIP-1 and RANTES chemokines with optimization for E.coli codon usage, was constructed by synthetic PCR (Gao et al., 2003). Enterokinase cutting site (DDDDK) was included before the first amino acid. 12 overlapping primers were designed by DNAworks 2.4 (Hoover and Lubkowski, 2002), with KpnI and Not I site flanking the 5' and 3' end. Synthetic MIP-1 cDNA were cloned into pET32a (Novagen) and verified by DNA sequencing. MIP-1α mutants were generated by site directed mutagenesis.

Chemokines were expressed as thioredoxin and His6 tag fusion proteins in BL21(DE3) cells. The fusion proteins were purified by Ni-NTA column as described previously (Guo et al., 2010) and further purified by a Source-Q column with an ascending NaCl gradient in the presence of 5mM EDTA.

Recombinant MIP-1 and RANTES proteins were obtained by removing fusion tags. 10 U of enterokinase (sigma) was combined with every mg fusion protein in 20mM Tris-HCl pH7.7, 5mM EDTA and incubated at 25□C for 16 hours. The reaction was desalted by PD-10 column (GE healthcare) then applied to Ni-NTA resin (Qiagen), non-binding fraction was collected then further purified by heparin affinity chromatography. Final products of MIP-1 were analyzed by MALDI-TOF

mass spectrometry, and its biological activity was assayed on THP-1 cells by chemotaxis assay (Fig. S1).

Wild type and mutant Human IDE proteins were expressed in E.coli Rosetta (DE3) with IPTG induction at 25□C for 16 hours. Recombinant IDE proteins were purified to homogeneity by Ni-NTA, Source-Q and Superdex S-200 columns as previously described (Im et al., 2007; Malito et al., 2008; Shen et al., 2006a).

Mass Spectrometry Analysis: For mass spectrometry analysis, enzyme reactions were carried out at 37°C by mixing equal volume of MIP-1 with IDE at the given molar ratio in the presence or absence of 0.8mg/ml heparin. 20μl reaction mixture was removed at indicated time, and stopped by 20μl stop buffer (200mM EDTA, 0.2% TFA). Samples were further incubated with 10mM TCEP at room temperature for 30 min to break the disulfide bonds and then subjected to either MALDI/TOF or LC-ESI-FTICR mass spectrometry analysis. For MALDI/TOF analysis, 10μl sample was purified by Zip-Tip C18 columns (Millipore), and applied to the metal plate with matrix (CHCA, in 70% ACN and 0.1% TFA). Mass spectra were obtained either in linear or positive reflector mode using a Voyager 4700 MALDI/TOF mass spectrometer (Applied Biosystems). For LC-ESI-FTICR-MS, MIP-1α samples (12μl) were injected into a nano RP-HPLC system (Dionex), with a C8 analytical column (Agilent). Peptides were eluted from the nano column with a linear gradient of 5-95% acetonitrile in 0.1% formic acid and sprayed into a LTQ-FT tandem MS instrument (Thermo Scientific). Spectra were acquired using positive ion nano ESI mode with the FTICR

acquiring precursor spectra from 200-2000 m/z. For tandem MS, precursor ions were fragmented by collision-induced dissociation (CID). MS/MS spectra were acquired in a data dependent manner from the 5 most intense precursor ions of each FTICR MS scan. The RAW data files are processed by Xtract™ function in Xcalibur™ (Thermo Fisher Scientific) to generate reduced data files containing the deconvoluted masses and intensities for MS spectra. For a reduced data file, all deconvoluted MS spectra are summed to create a single pseudo-MALDI TOF mass spectrum by use of an in-house developed program written in Python. In brief, the peaks in all MS spectra are merged and peaks with m/z values matching within 5 ppm are summed into a single peak with the summed intensity. MS and tandem MS/MS data were analyzed by online tools, FindPept (http://ca.expasy.org/tools/findpept.html), Mascot (http://www.matrixscience.com/search_form_select.html) and MassMatrix (http://www.massmatrix.net) (Xu and Freitas, 2009).

The confirmation of MIP-1α degradation products by ^{18}O water labeling: This technique utilizes a protease enzyme reaction in ^{18}O water to produce isotope-labeled peptides. ^{18}O labeling will result in 2Da mass addition, which can be resolved by comparing the isotope envelope pattern to ^{16}O samples. In contrast, any pre-existing fragments will not be modified and have identical isotope distribution. In our IDE-digested MIP-1α spectra, all 8 fragments that represent the initial cleavage products (1-18 and 19-70, 1-45 and 46-70, 1-46 and 47-70, 1-48 and 49-70) could be identified. Peptides 1-18, 1-45, 1-46 and 1-48 were labeled with ^{18}O as shown by a mass shift in the isotope distribution;

while the other four peptides 19-70, 46-70, 47-70 and 49-70 were not labeled (Table S3, Figure S11).

Size exclusion chromatography: Purified human MIP-1 samples dialysis against phosphate buffer saline (PBS) pH 7.4 with or without 0.1mg/ml heparin, then concentrated to 1mg/ml using a centrifugal filter device (AmiconUltra4 3 kDa MWCO, Millipore). 100ul the concentrated protein was applied to an equilibrated Superdex200 10/300 GL size exclusion chromatography column. PBS with or without 0.1mg/ml heparin was used for equilibration of the column as well as for elution. The molecular mass standards used are thyroglobulin (670 kDa), γ-globulin (158 kDa), ovalbumin (44 kDa), myoglobin (17 kDa) and vitamin B12 (1.35 kDa).

The modeling of reversible MIP-1 polymers and fit to the experimental data: The modeling of SAXS data was based on the RA_2 model of van Dongen and Ernst (van Dongen and Ernst, 1984). At equilibrium, the concentration of k-mers, c_k should read $c_k = \frac{c_t}{2}(1-\alpha)^2 \alpha^{k/2-1}$ where k can only be an even integer, c_t is total MIP-1 monomer concentration, and $\alpha = 1 + \frac{K_d}{c_t} - \sqrt{\left(\frac{K_d}{c_t}\right)^2 + \frac{2K_d}{c_t}}$. Here, K_d is the equilibrium dissociation constant for a dimer-dimer bond. This predicts that the average degree of polymerization is $2 \bullet \left(\frac{1+\alpha}{1-\alpha}\right)$, which depends on c_t. The theoretical scattering curves for uniform length polymers were calculated using Crysol and then combined into the scattering curves expected for a polymer distribution using Matlab. Fits to the experimental data were performed using

Matlab and included three adjustable parameters: a constant scattering background, the total scattered intensity and either the polymer length (for single-length fits) or the parameter α (for polymer length distribution fits). Denoting by $I^{\alpha}_{theo}(q)$ the theoretically expected scattering intensity for a polydisperse polymer solution characterized by the parameter α with the normalization condition $I^{\alpha}_{fit}(0)=1$, we fitted the experimental curves by minimizing the fit function $\int_0^{q_{\max}} [I_0 \times I^{a}_{theo}(q) - I_{\exp}(q) + I_b]^2 \, dq/q_{\max}$ with respect to α, the zero-angle scattered intensity I_0 and a q-independent background intensity I_b. Here $q_{\max}$ is the largest scattering wavevector for which data was collected. A similar procedure was used for the monodisperse polymer solution fit, where the adjustable parameter α is replaced by L, the polymer length. The fitting errors $I_0 \times I^{a}_{theo}(q) - I_{\exp}(q) + I_b$ are represented in the deviation curve.

MIP-1α competition assay: MIP-1α competition assay was performed as previously described. IDE enzyme activities were assayed using substrate V (7-Methoxycoumarin-4-yl-acetyl-NPPGFSAFK-2,4-dinitrophenyl) (Manolopoulou et al., 2009; Shen et al., 2006b). 85μl of 0.35 μM substrate V was mixed with 10μl of MIP-1α at various concentrations. The reactions were initiated by addition of 5μl of IDE protein (0.2mg/ml), carried out at 37°C for 15min. The substrate V degradation was monitored by fluorescence intensity on a Tecan Safire microplate reader with excitation and emission wavelengths at 327nm and 395nm respectively. Data were plotted and analyzed with PRISM software (Graphpad).

Cellular Assays: IDE expression in BV-2 cells is knockdown by lenti-virus mediated shRNA expression. A set of 5 plasmids which encode shRNA targeting mouse IDE gene were purchased from Open Biosystem (RMM4534-NM-031156). Lenti-virus were produced by co-transfecting shRNA plasmids with pHR8.2ΔR packaging plasmid and pCMV VSVG envelope plasmid into HEK293T cells. Virus containing media was harvested 48hr post transfection. BV-2 cells were infected with virus for 24 hours in the presence of 8ug/ml polybrene, and then stable lines were obtained by 2-week selection with 5ug/ml puromycin. IDE knockdown levels were confirmed by western blotting with a polyclonal anti-IDE antibody. Secreted MIP-1 level from IDE knockdown BV-2 cells were measured by ELISA assays. Stable BV-2 cells lines were seed at $2.5x10^4$/well in 24-well plate one day before the assay. Fresh culture media with or without 10ng/ml LPS was changed (0.5ml/well) and after 3 hours incubation at 37°C media harvested. Chemokine levels in these samples were measured by anti-mouse MIP-1α, MIP-1β and RANTES ELISA kits (R&D system) according to manufactures instruction. Chemokine concentrations (pg/ml) were calculated from the standard curve measured within the same assay.

Chemotaxis Assay: Cell migration was measured in 96-well Multiscreen™ filter plate (Millipore) as described in (Gouwy et al., 2008). Cytokines were diluted into the assay medium (RPMI 1640 without phenol red, supplemented with 10mM HEPES pH7.4, 0.1% heat inactivated BSA) at indicated concentration. 150µl sample was placed in the lower well of 96-well receiver plate. THP-1 cells were washed once with dPBS, then resuspended in assay medium at a concentration

of $2.5x10^6$/ml. 100ul cell suspension was loaded into upper wells of 96-well filter plate (5μm pore size). Cells were allowed to migrate for 3 hrs at 37°C. After removing the upper 96-well filter plate, the cell number in the lower receiver plate were quantified using the ATPlite™ luminescence assay system (PerkinElmer) according to manufacturer's instruction. The chemotaxis index was calculated by dividing the luminescence values of the sample over assay medium alone.

Calcium Mobilization Assay: THP-1 cells were washed once, and then loaded with 2μM fura-2 AM (Invitrogen) in assay medium (same as chemotaxis assay) at 37°C for 30min. Subsequently, cells were washed once with dPBS then resuspended in assay medium at 10^6 cell/ml. 2ml fura-2 loaded cell suspension was transferred to a cuvette with a magnetic stirring bar. Fura-2 fluorescence was measured with a FluoroMax-3 fluorometer (HORIBA Jobin Yvon Inc.) at excitation wavelengths of 340 and 380 nm and emission wavelength of 510 nm. MIP-1α incubated with or without IDE were diluted into the assay medium, and added into cell suspension at indicated concentration.

Figure Legends

Figure S1 The assessment of recombinant MIP-1 proteins (A) WT MIP-1α, (B) WT MIP-1α (purchased from Peprotech), (C) WT MIP-1β, (B) WT MIP-1β(purchased from Peprotech), (E) MIP-1α L3M V63M, (F) MIP-1α D27A (G) RANTES and (H) MIP-1α P8A in their purity by MALDI-TOF MS spectrum and in their *in vitro* chemotactic activity using THP-1 cells. Chemotactic response was expressed as mean chemotaxis index, and shown as the *insert* graph.

Figure S2 Density of the MIP-1 protein and complex of IDE_CF_E111Q with MIP-1α. (A) the $2f_o$-f_c map of the MIP-1 proteins at 2.5δ level; (B). The composite omit map of the MIP1a in complex of IDE/MIP-1α at 1.5δ

Figure S3 The structure comparison of CCL chemokine structures. MIP-1α crystal structure from our MIP-1α polymer structure is compared with CCL family protein structures that are (A) monomer, (B) dimer, (C) tetramer available from RCSB database. The monomers in the dimer and tetramer were colored differently. The PDB codes are as listed.

Figure S4 Structure analysis of the dimer interaction of MIP-1α (**S4-1**), MIP-1β (**S4-2**) as well as that between IDE and MIP-1α (**S4-3**). In **Figure S4-1** and **S4-2**, (A) Details of the hydrogen bond and salt bridge built between different monomers. (B) The accessible surface area (ASA) and buried surface area (BSA) of the interfacing residues between monomers. (C) The buried interface area between monomers. The area was calculated through the PISA server

(http://www.ebi.ac.uk/msd-srv/prot_int/cgi-bin/pisever). The monomer designation (A-D) is indicated in the figure on the right.

Figure S5 The sequence alignment of the CCL proteins (A) and phylogenic tree of CCL proteins (B). The key residues involving MIP1α dimer contact were colored red as the cysteine colored green.

Figure S6 p(r) function distributions for 1mg/ml MIP-1 proteins without (left) or with (right) 0.1mg/ml heparin. With the use of a q-range of 0.0068 to 0.343, a maximum dimension (D_{max}) and the interatomic distance distribution functions p(r) were computed by GNOM.

Figure S7 SEC analysis of various concentrations of (A) MIP-1α, (B) MIP-1β and (C) MIP-1α P8A. SEC was performed on S-200 column in phosphate-buffered saline (PBS). The elution volume of molecular standard proteins is indicated by the dotted lines.

Figure S8 Comparison of the MIP-1α and MIP-1β experimental SAXS data (black) with the theoretical scatting patterns from a single length polymer (green) or a polymer length distribution as calculated from our model (red). The size distribution of mass from polymer distribution is shown as an inset and the fitting error is shown under the fitting curve. The fitting errors $I_0 \times I^a_{theo}(q) - I_{\exp}(q) + I_b$ are represented in the deviation curve. The D values from the fit function $\int_0^{q_{\max}} [I_0 \times I^a_{theo}(q) - I_{\exp}(q) + I_b]^2 \, dq/q_{\max}$ for single length and polymer distribution are listed. Inset: size distribution of the polymers length distribution.

Figure S9 MIP-1α mediated intracellular calcium response in THP-1 cells. (A) Dose-dependent changes of intracellular calcium concentrations by MIP-1α. Fura-2 loaded THP-1 cells were stimulated with the indicated concentrations of MIP-1α. Stimulus dependent $[Ca^{2+}]_i$ changes were monitored by ratio of fluorescence at 340nm over 380nm. The change of $[Ca^{2+}]_i$ is indicated by ΔF340/F380 which is the difference between the peak F340/F380 value after addition of MIP-1α and basal level before stimulation. (B) MALDI-TOF-MS spectra of IDE digested MIP-1α samples used in examining the effect of the degradation of MIP-1α by IDE (Figure 5C).

Figure S10 Comparison of mass spectra of IDE digested MIP-1α peptides in $H_2{}^{18}O$ and $H_2{}^{16}O$. IDE digested MIP-1α peptides were analyzed by LC-ESI-FTICR MS. The spectra from digestion in $H_2{}^{16}O$ are shown in red; spectra from digestion in 50% $H_2{}^{18}O$ are shown in blue. Spectra from the same peptide fragments are overlaid and shown as (A) residues 1-48, (B) residues 49-70, (C) residues 1-46, (D) residues 47-70 and (E) residues 1-70.

Figure S11 Model of catalysis mechanism for IDE. MIP-1α is depicted as red; IDE-N and IDE-C are depicted as light blue and grey surfaces, respectively. IDE^o is theoretically modeled based on the substrate free *E. coli* pitrilysin (1Q21); IDE^c corresponds to the atomic coordinate of IDE-CF-E111Q-MIP-1α (3H44). The detail description of mechanism is in the discussion.

Reference

Gao, X., Yo, P., Keith, A., Ragan, T. J., and Harris, T. K. (2003). Thermodynamically balanced inside-out (TBIO) PCR-based gene synthesis: a novel method of primer design for high-fidelity assembly of longer gene sequences. Nucleic Acids Res *31*, e143.

Gouwy, M., Struyf, S., Noppen, S., Schutyser, E., Springael, J. Y., Parmentier, M., Proost, P., and Van Damme, J. (2008). Synergy between coproduced CC and CXC chemokines in monocyte chemotaxis through receptor-mediated events. Mol Pharmacol *74*, 485-495.

Guo, Q., Manolopoulou, M., Bian, Y., Schilling, A. B., and Tang, W.-J. (2010). Molecular Basis for the Recognition and Cleavages of IGF-II, TGF-α, and Amylin by Human Insulin-Degrading Enzyme. Journal of Molecular Biology *395*, 430-443.

Hoover, D. M., and Lubkowski, J. (2002). DNAWorks: an automated method for designing oligonucleotides for PCR-based gene synthesis. Nucleic Acids Res *30*, e43.

Im, H., Manolopoulou, M., Malito, E., Shen, Y., Zhao, J., Neant-Fery, M., Sun, C. Y., Meredith, S. C., Sisodia, S. S., Leissring, M. A., and Tang, W. J. (2007). Structure of substrate-free human insulin-degrading enzyme (IDE) and biophysical analysis of ATP-induced conformational switch of IDE. J Biol Chem *282*, 25453-25463.

Malito, E., Ralat, L. A., Manolopoulou, M., Tsay, J. L., Wadlington, N. L., and Tang, W.-J. (2008). Molecular bases for the recognition of the short peptide substrate and cysteine-directed modifications of human insulin-degrading enzyme. Biochemistry *47*, 12822-12834.

Manolopoulou, M., Guo, Q., Malito, E., Schilling, A. B., and Tang, W. J. (2009). Molecular basis of catalytic chamber-assisted unfolding and cleavage of human insulin by human insulin-degrading enzyme. J Biol Chem *284*, 14177-14188.

Shen, Y., Joachimiak, A., Rosner, M. R., and Tang, W.-J. (2006a). Structures of human insulin-degrading enzyme reveal a new substrate recognition mechanism. Nature *443*, 870-874.

Shen, Y., Joachimiak, A., Rosner, M. R., and Tang, W. J. (2006b). Structures of human insulin-degrading enzyme reveal a new substrate recognition mechanism. Nature *443*, 870-874.

van Dongen, P. G. J., and Ernst, M. H. (1984). Kinetics of reversible polymerization. J Stat Phys *37*, 301-324.

Xu, H., and Freitas, M. A. (2009). MassMatrix: a database search program for rapid characterization of proteins and peptides from tandem mass spectrometry data. Proteomics *9*, 1548-1555.

Polymerization of human MIP-1 chemokines (CCL3 and CCL4) and clearance of MIP-1 by human insulin degrading enzyme

—

supplemental mathematical modeling

Ren *et al.*

1 Equilibrium polymer length distribution

1.1 Description of the polymerization model

Here we describe the polymerization model used in the main text. This model is the equilibrium version of the RA_2 model of Ref. [1]. We use it to describe a solution of MIP-1 dimers with concentration $c_t/2$ (*i.e.*, c_t is the total monomer concentration). These dimers can reversibly assemble into linear polymers according to the following scheme:

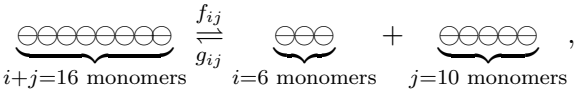

(1)

where f_{ij} and g_{ij} are the kinetic dissociation and association rates, respectively. Note that here each circle represents a dimer, *i.e.*, two monomers. In this approach, we assume that the MIP-1 dimer concentration is much larger than the dissociation constant corresponding to the dissociation of a dimer into monomers. Therefore we assume that only dimers or polymers of dimers are present throughout this section[1]. As a consequence, i and j are assumed to be even integers in all the following.

The approach of Ref. [1] relies on two main assumptions:

- No circular polymers are formed. This is reasonable if the persistence length of the polymers (the typical length over which they bend due to thermal fluctuations) is much larger than their contour length.
- Identical chemical groups have *a priori* equal chemical reactivity. This means that the kinetic association constant g_{ij} in the reaction pictured in Eq. (1) is independent of i and j: $g_{ij} = g$. This is reasonable in the limit of long polymers. Indeed, in this limit the reactivity of the polymer's end groups should go to a well-defined constant.

[1]The assumption that most of MIP-1 are either dimers or polymers is likely fulfilled in our SAXS experiments where $\sim 100\,\mu$M MIP-1 was used, and the dimerization constant of MIP-1 is estimated to be in nM range. Note however that relaxing this assumption, *i.e.*, taking the equilibrium between monomers and dimers into account does not modify the form of the polymer length distribution. Essentially, there is an effective dimer concentration lower than c_t, because a fraction of MIP-1 is monomeric.

1.2 Additional conditions

Assuming a constant g as discussed in the previous section, we enforce two additional conditions and deduce the value c_k of the equilibrium concentration of k-mers (polymers comprising k monomers).

1. *Normalization condition.* This requires that the total fragmentation rate of a k-mer be proportional to the number of dimer-dimer bonds in this k-mer. Since there are $k/2$ dimers in the k-mer, this number of bonds is equal to $k/2-1$. Similar to the above, this is expected in the limit of long polymers, as in this limit most fragmentation events occur deep within the polymer. At the locations of these events, the ends of the polymer are far enough from the fragmentation site for the fragmentation rate to be independent of their location. In other words, we assume that all bonds are equally breakable, in agreement with the assumption of *a priori* equal chemical reactivity. This condition reads:

$$\frac{1}{2}\sum_{i+j=k \text{ even}} f_{ij} = \lambda\left(\frac{k}{2}-1\right), \tag{2}$$

   where λ is a proportionality constant and where the sum runs over all strictly positive even integers i and j whose sum is k (also an even integer).

2. *Detailed balance condition.* In a stationary state the number of k-mers lost to the i- and j-mers through fragmentation is exactly compensated by the number of k-mers formed out of i- and j-mers:

$$f_{ij}c_{i+j} = g_{ij}c_ic_j = gc_ic_j, \tag{3}$$

   where the assumption $g_{ij}=g$ discussed in the previous section was used.

1.3 Equilibrium distribution

Combining Eqs. (2) and (3) and noting that $c_{i+j}=c_k$ for all terms in the sum, we obtain

$$\lambda\left(\frac{k}{2}-1\right)c_k = \frac{g}{2}\sum_{i+j=k \text{ even}} c_ic_j. \tag{4}$$

It can easily be checked by substitution into Eq. (4) that the solution of this recursion reads

$$c_k = \frac{2\lambda}{g}\left(\frac{gc_2}{2\lambda}\right)^{k/2}, \tag{5}$$

where the dimer concentration c_2 remains to be determined. This is done by imposing that the total monomer concentration in the solution is equal to c_t, which reads

$$c_t = \sum_{k=2,4,6,\ldots\infty} kc_k = \frac{4\lambda}{g}\left(c_2\frac{\mathrm{d}}{\mathrm{d}c_2}\right)\sum_{l=1}^{+\infty}\left(\frac{gc_2}{2\lambda}\right)^l, \tag{6}$$

where we made the change of dummy variable $l=k/2$, which implies that the sum over l runs over all strictly positive integers. We can sum the geometric series in Eq. (6), noting that its convergence requires $gc_2/2\lambda<1$:

$$c_t = \frac{2c_2}{(1-gc_2/2\lambda)^2}. \tag{7}$$

We solve this quadratic equation for c_2, which yields two solutions. One of these is such that $gc_2/2\lambda > 1$, which is unphysical as discussed above [this corresponds to a diverging series in Eq. (6), and therefore to an infinite total concentration]. The other solution is always well-behaved, and reads

$$\alpha = \frac{gc_2}{2\lambda} = 1 + \frac{2\lambda}{gc_t} - \sqrt{\left(\frac{2\lambda}{gc_t}\right)^2 + \frac{4\lambda}{gc_t}}. \tag{8}$$

1.4 Dimer-dimer dissociation constants

We define the equilibrium dissociation constant associated with the reaction Eq. (1) as

$$K_d(i,j) = \frac{c_i c_j}{c_{i+j}}. \tag{9}$$

Substituting the expression of Eq. (5) for the concentrations into this equation, we find that K_d does not depend on i and j, which reflect the fact that all bonds are treated as identical (they all have the same binding energy). In particular, K_d is equal to the dissociation constant of a tetramer into two dimers, and thus characterizes the binding affinity between MIP-1 dimers. It reads

$$K_d = \frac{2\lambda}{g}. \tag{10}$$

Combining Eqs. (3) and (9), we find that f_{ij} does not depend on i and j either and reads

$$f = gK_d. \tag{11}$$

Substituting Eq. (10) in Eqs. (5) and (8), we rewrite our polymer length distribution as a function of only two parameters: the binding affinity K_d between MIP-1 dimers and the total MIP-1 concentration c_t:

$$c_k = \frac{c_t}{2}(1-\alpha)^2\alpha^{k/2-1} \quad \text{with} \quad \alpha = 1 + \frac{K_d}{c_t} - \sqrt{\left(\frac{K_d}{c_t}\right)^2 + \frac{2K_d}{c_t}}, \tag{12}$$

where $0 \leqslant \alpha < 1$. Therefore the fraction c_k/c_t of polymers of length k depends on K_d/c_t only.

1.5 Discussion of the length distribution and average polymer length

To get a better feeling of the meaning of this distribution, we now turn our interest to the fraction of the total MIP-1 mass that is included in k-mers. We note that the mass comprised in k-mers is proportional to kc_k, *i.e.*, the number of monomers in each k-mer. Moreover, the total number of MIP-1 monomers is c_t, and therefore

$$\text{mass fraction}(k) = \frac{kc_k}{c_t} = \frac{k(1-\alpha)^2\alpha^{k/2-1}}{2}. \tag{13}$$

Interestingly, the relative mass distribution specified by this expression is a function of only one quantity: the ratio K_d/c_t of the dimer-dimer dissociation constant to the total monomer concentration. We illustrate this dependence in Fig. SM1.

To quantify the typical polymer size associated with the curves presented in this figure, we calculate the average of the distribution of Eq. (13). This quantity is also known as the degree of

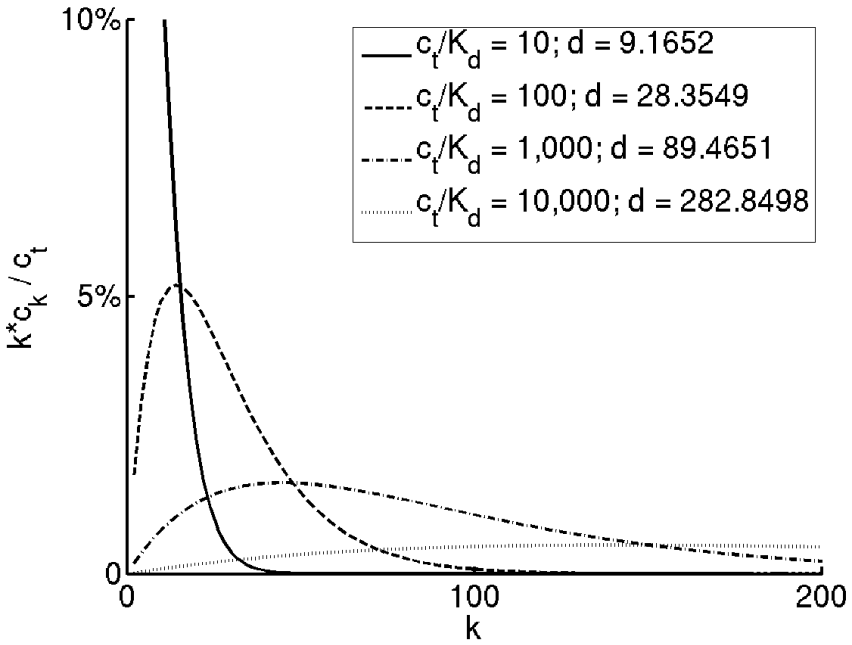

Figure SM1: Plots of the mass fraction of k-mers as expressed in Eq. (13) as a function of k for different values of the ratio c_t/K_d. In each case, the average degree of polymerization [Eq. (14)] is indicated in the legend. Since the distribution depends only on the ratio of c_t and K_d, the solid curve might represent the distribution for $c_t = 100\,\mu$M and $K_d = 10\,\mu$M just as well as the situation $c_t = 30\,\mu$M and $K_d = 3\,\mu$M. The same type of comment holds for the other curves. Qualitatively, the average polymer size as well as the width of the size distribution increase for both increasing c_t (putting more monomers displaces the equilibrium towards the more associated forms) and decreasing K_d.

polymerization and reads:

$$\begin{aligned} d(\alpha) &= \sum_{k \text{ even}} k \times \text{mass fraction}(k) \\ &= \frac{2(1-\alpha)^2}{\alpha} \sum_{l=1}^{+\infty} l^2 \alpha^l \\ &= \frac{2(1-\alpha)^2}{\alpha} \left(\alpha \frac{\mathrm{d}}{\mathrm{d}\alpha}\right)^2 \sum_{l=1}^{+\infty} \alpha^l \\ &= 2\left(\frac{1+\alpha}{1-\alpha}\right). \end{aligned} \tag{14}$$

This measure of the polymer length can help us qualitatively understand the meaning of the dissociation constant K_d for the polymerization process. We see from Eq. (9) that K_d is expressed in units of concentration—it actually represents the characteristic concentration for the onset of polymerization. More specifically, if $c_t = 3K_d/2$, then $\alpha = 1/3$ and $d(\alpha) = 4$, meaning that the MIP-1 molecules are typically in the tetramer form. Lower values of c_t yield mostly dimeric MIP-1, and higher values lead to longer polymers.

The degree of polymerization $d(\alpha)$ is also related to the position of the peak of the distributions pictured in Fig. SM1. Indeed, this peak is characterized by

$$\frac{\mathrm{d}[\text{mass fraction}(k)]}{\mathrm{d}k} = 0 \quad \Leftrightarrow \quad k = k_{\text{peak}}(\alpha) = -\frac{2}{\ln(\alpha)} \tag{15}$$

Thus the following relationship between $d(\alpha)$ and $k_{\text{peak}}(\alpha)$ holds:

$$d(\alpha) = 2 \times \frac{1 + \exp\left[-2/k_{\text{peak}}(\alpha)\right]}{1 - \exp\left[-2/k_{\text{peak}}(\alpha)\right]} \sim 2k_{\text{peak}}(\alpha) \quad \text{as} \quad k_{\text{peak}} \to +\infty. \tag{16}$$

Therefore, for long polymers, the degree of polymerization is equal to twice the length of the most abundant species.

2 Chemokine gradient in the presence of polymerization

2.1 Description of the model

To better understand the interplay between MIP-1 degradation and its dimerization and polymerization in the formation of a spatial chemotactic gradient, we supplement the model of the previous section with the following reactions:

$$(\text{dimer}) \underset{k_a}{\overset{k_d}{\rightleftharpoons}} (\text{monomer}) + (\text{monomer}) \quad \text{and} \quad (\text{monomer}) \xrightarrow{r} \text{degradation}, \tag{17}$$

which account for MIP-1 dimerization and degradation. Only monomers are subject to degradation by the protease IDE, as discussed in the main text. The constant degradation rate r assumes a constant concentration of IDE in the region of interest.

We also describe the spatial structure of the MIP-1 gradient, and take into account the diffusion of the different MIP-1 species in a one-dimensional medium parametrized by the spatial coordinate x. For simplicity, we assume that they all have the same diffusion constant D. This yields the following rate equations for the concentrations of the various MIP-1 constructs:

$$\text{monomers:} \quad \frac{\partial c_1}{\partial t} = D\frac{\partial^2 c_1}{\partial x^2} - k_a c_1^2 + k_d c_2 - r c_1 \tag{18a}$$

$$\text{dimers:} \quad \frac{\partial c_2}{\partial t} = D\frac{\partial^2 c_2}{\partial x^2} + \frac{k_a}{2} c_1^2 - \frac{k_d}{2} c_2 - \sum_{i=2,4,6\ldots} (g c_2 c_i - f c_{2+i}) \tag{18b}$$

$$k>2 \text{ polymers:} \quad \frac{\partial c_k}{\partial t} = D\frac{\partial^2 c_k}{\partial x^2} + \frac{1}{2} \sum_{i+j=k \text{ even}} (g c_i c_j - f c_{i+j}) - \sum_{i=2,4,6\ldots} (g c_k c_i - f c_{k+i}) \tag{18c}$$

where the concentrations are now taken to be space- and time-dependent and $c_1(x,t)$ is the monomer concentration. We consider a geometry corresponding to the physiological situation of a large[2] wound located in the $x = 0$ plane. Dendritic cells in the vicinity of this plane would start secreting MIP-1 at a constant rate J, which would then penetrate into the tissue in the direction of positive xs. No MIP-1 dimers or polymers go into or out of the $x = 0$ plane, and we demand that the chemokine concentration vanishes far away from the secretion site. This situation is described by the following boundary conditions:

$$D\frac{\partial c_1}{\partial x}(x=0) = -J, \quad D\frac{\partial c_k}{\partial x}(x=0) = 0 \text{ for all } k>1 \quad \text{and} \quad c_k(x=+\infty) = 0 \text{ for all } k. \tag{19}$$

[2] In this context, "large" means larger than the depth of the MIP-1 gradient, which is typically 1 mm as discussed below.

2.2 Estimation of the parameters

In the following we assume that the diffusion constant for all MIP-1 species is of order $D = 1\,\mu\mathrm{m}^2\,\mathrm{s}^{-1}$, which is a typical value for objects with a size of order 10 nm in a medium ten times more viscous than water (this was estimated using the Stokes-Einstein formula—the increased viscosity compared to water is meant to account for the crowded environment of the tissue considered).

According to the main text, MIP-1 forms polymers with a typical degree of polymerization $d(\alpha) = 40$ when a total MIP-1 concentration $c_t \simeq 100\,\mu\mathrm{M}$ is used. Using Eq. (14), we find that this corresponds to $\alpha \simeq 0.95$. Combining Eqs. (7) and (10), this implies

$$K_d = \frac{(1-\alpha)^2}{2\alpha} c_t \simeq 100\,\mathrm{nM}. \tag{20}$$

In the following we assume that $f = 10^{-2}\,\mathrm{s}^{-1}$, a value chosen to yield a physiologically reasonable chemokine penetration depth of order 1 mm. Substituting into Eq. (11) yields $g = 10^5\,\mathrm{M}^{-1}\,\mathrm{s}^{-1}$.

Consistent with the assumptions of the main text and the discussion of footnote 1, we assume that the dissociation constant $K'_d = k_d/k_a$ for the MIP-1 dimerization reaction is much smaller than K_d. Here we choose $K'_d = K_d/10 = 10\,\mathrm{nM}$. We also choose $k_d = f = 10^{-2}\,\mathrm{s}^{-1}$, which implies $k_a = 10^6\,\mathrm{M}^{-1}\,\mathrm{s}^{-1}$.

As described above, the source of MIP-1 in our model is the $x = 0$ plane, which can be thought of as a surface onto which MIP-1-secreting dendritic cells are grafted. Assuming that the typical inter-cell distance in this plane is of order $30\,\mu\mathrm{m}$ and using a MIP-1 secretion rate of $1\,\mathrm{pg}\,\mathrm{s}^{-1}$ as reported in Ref. [2], we calculate that the secretion of MIP-1 per unit time per unit area in the plane is approximately $J = 2 \times 10^{-11}\,\mathrm{mol}\,\mathrm{m}^{-2}\,\mathrm{s}^{-1}$.

Finally, we assume that MIP-1 degradation by IDE is slow compared to the other reactions described here. Note that if this were not the case and degradation were fast, all the chemokine would be degraded before having the time to dimerize or polymerize. We choose $r = f/10 = 10^{-3}\,\mathrm{s}^{-1}$, meaning that a monomer is typically degraded 1000 s after having been secreted. Given the fact that IDE typically degrades a MIP-1 monomer in a time of order 1 s (see main text), this assumption yields rates consistent with an IDE concentration equal to one thousandth of the typical MIP-1 monomer concentration. In the next section we show that the assumptions described here yield MIP-1 monomer concentrations of the order of 100 nM, which implies concentrations of IDE in the 100 pM range.

According to these considerations, our model comprises only one arbitrarily chosen parameter k_d. Moreover, the value of this rate constant has little influence on the results presented in the next section as long as it is significantly larger than r. Our model can thus be expected to offer some valuable insight into the physiological situation.

2.3 Results

We evolve the reaction-diffusion equations Eqs. (18) and (19) numerically starting from a situation where all concentrations are zero until a steady-state is reached. In Fig. 4A of the main text and in the following we present the results from three different situations, which illustrates the role of MIP-1 dimerization and polymerization in the shaping of a chemotactic gradient:

1. *Monomers only.* The numerical values of Sec. 2.2 are used, except for k_a, which we set to zero. This prevents the formation of any dimers or polymers, and yields an exponential decay of the chemotactic gradient which is described by the analytical formula

$$c_1(x, t = +\infty) = \frac{J}{\sqrt{r}} e^{-\sqrt{r}x}. \tag{21}$$

2. *Monomers and dimers.* The numerical values of Sec. 2.2 are used, except for g, which we set to zero. This prevents the formation of any polymers, but allows for dimers. The resulting steady-state monomer and dimer concentration profiles are shown in Fig. SM2(a)

3. *Monomers, dimers and polymers.* All numerical values of Sec. 2.2 are used, meaning that monomers, dimers and polymers are all present.The resulting steady-state concentration profiles are shown in Fig. SM2(b), and the average degree of polymerization of the polymers as a function of x is illustrated in Fig. SM2(c).

In the following we assume that only the MIP-1 monomer has a chemotactic activity, in agreement with Ref. [3]. It is thus interesting to compare the monomer concentration profiles for the three cases considered, which we do in Fig. SM2(d).

One common feature of the "monomers and dimers" and the "monomers, dimers and polymers" profiles plotted in this figure is a boundary region with a steep slope for small ($< 10\,\mu$m) values of x. This is due to the fact that the source in $x = 0$ produces only monomers. Shortly after having been secreted, these monomers react together to form dimers and polymers, hence a decrease in the monomer concentration. Since these aggregation reactions are much faster than the monomer degradation, the amount of monomers degraded in this region is negligible, and the ratios between the various concentrations are locally close to their equilibrium values. Had we assumed that the dendritic cells secrete not monomers, but a mixture of dimers and polymers, those species would also have reached chemical equilibrium within $\sim 10\,\mu$m of the secretion site, and therefore the shape of the chemotactic gradient outside of that region would be much the same as the one presented here.

There are three noteworthy consequences of MIP-1 aggregation, all of which are more pronounced in the "monomers, dimers and polymers" case than in the "monomers and dimers" case:

- the monomer concentration for small x is reduced compared to the "monomers only" case, due to the assembly of the monomers into higher-order aggregates.

- the slope of the monomer profile is reduced, especially for small x, as degradation proceeds at a slower rate because of the smaller monomer concentration and also because the monomer pool is constantly replenished through the disassembly of the higher-order aggregates.

- the chemotactic gradient reaches further away from the secretion point, which could enable the recruitment of macrophages from a longer distance.

Interestingly, the MIP-1 profile plateaus at intermediate distances in the "monomers, dimers and polymers" case, which suggests that macrophages in this region might not be directed to the inflammation site, but would rather undergo random motion. More quantitatively, it has been reported that chemotaxis can occur only if the chemoattractant concentration drops by more than a quantity of order 1% across the cell length [4, 5]. Denoting the cell size by $a \simeq 10\,\mu$m, this can be expressed mathematically by

$$\frac{c(x) - c(x+a)}{c(x)} > 1\% \quad \Leftrightarrow \quad \left| \frac{1}{c} \frac{\partial c}{\partial x} \right| > \frac{1}{100a} \simeq 10^3\,\mathrm{m}^{-1}, \tag{22}$$

where the equivalence holds if the chemotactic gradient is smooth on length scales of the order of a. As reported in Fig. 4A of the main text, we applied this criterion to the profiles calculated in the "monomers, dimers and polymers" case, and found that the gradient can induces chemotaxis only for[3] $x > 530\,\mu$m.

[3] In the example considered here, the "monomers only" and "monomers and dimers" cases yield chemoattraction for all values of x. Note that the boundary region $x < 10\,\mu$m is not considered in this discussion.

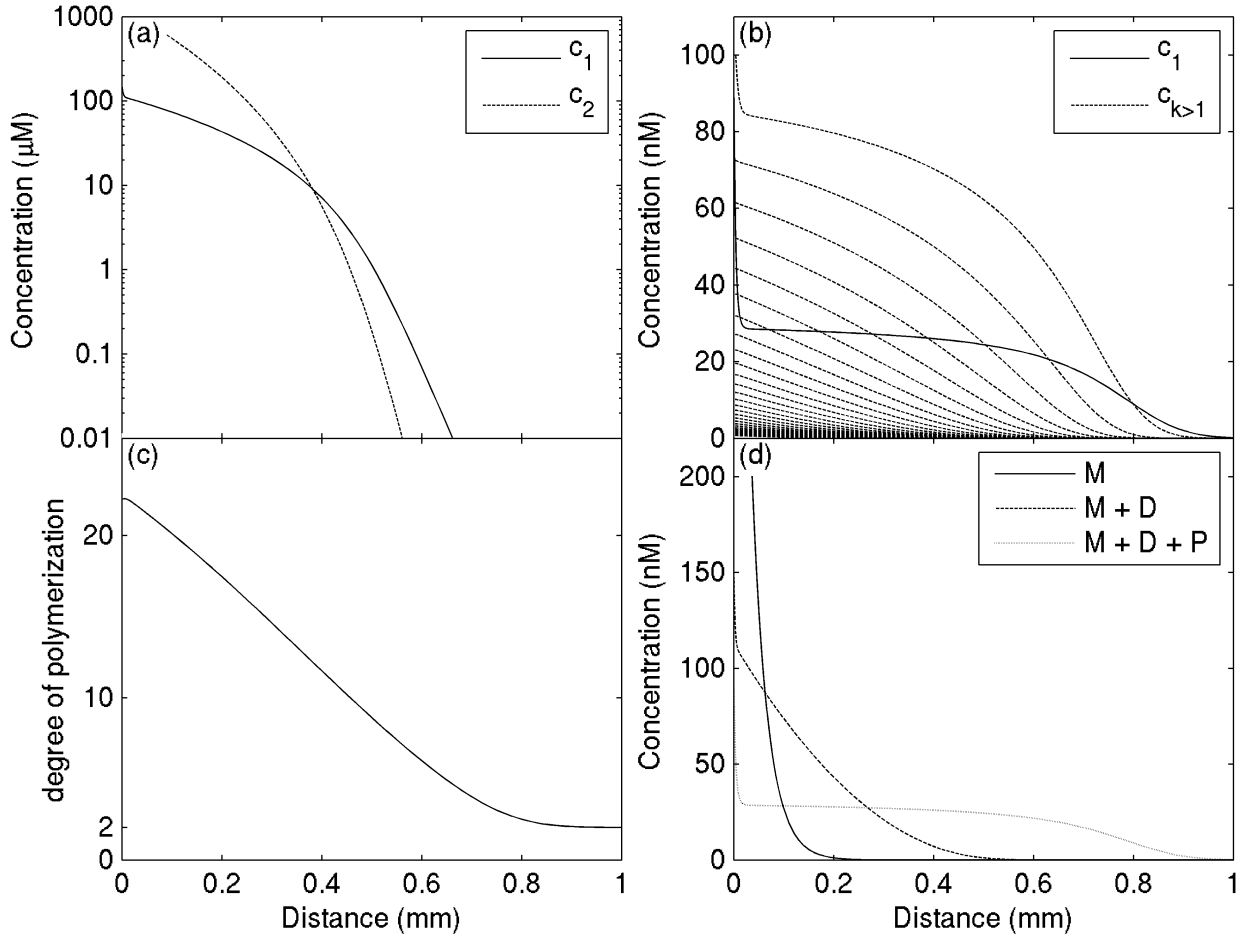

Figure SM2: MIP-1 concentration profiles as calculated from our model. (a) linear-logarithmic plot of the monomer (solid line) and dimer (dashed line) steady-state concentration profiles in the absence of polymerization. Note that most MIP-1 is in its dimer form for small x, *i.e.*, where large concentrations of MIP-1 are present. MIP-1 degradation is considerably hindered in these regions as only a small fraction of the MIP-1 (the monomeric fraction) is accessible to degradation. In regions where the total MIP concentration is smaller than K'_d, monomers are predominant and degradation proceeds unabated. (b) linear-linear plot of the monomer (solid line) and polymer (dashed line) steady-state concentration profiles. The uppermost dashed line represents the dimer concentration, the second one the tetramer concentration, the third the hexamer concentration and so on. (c) Average degree of polymerization as a function of x for the data presented in (b). Highly polymerized forms of MIP-1 dominate for small x and disappear as the chemokine is slowly degraded. Beyond $x = 800\,\mu$m, dimers are the dominant aggregated form of MIP-1, although it is seen in (b) that they are less abundant than monomers. (d) Comparison between the monomer concentrations in the three cases enumerated in Sec. 2.3 as in Fig. 4A of the main text, but using a linear-linear scale instead of a linear-logarithmic one.

These effects might be relevant for macrophage recruitment *in vivo*. Since dimerization and polymerization occur only when a relatively large concentration of MIP-1 is present, we would expect them to preferentially happen following a severe infection. In this situation it could be physiologically profitable to target macrophages to an extended region surrounding the infection site rather than directing them to its exact location. Also, the chemotactic gradient is more extended when polymerization occurs, which would allow the recruitment of macrophages from a wider area, thus providing a more dramatic response to the infection.

References

[1] P G J van Dongen and M H Ernst. Kinetics of reversible polymerization. *J. Stat. Phys.*, 37(3–4):301–324, 1984.

[2] Federica Sallusto, Alfonso Martín-Fontecha, and Antonio Lanzavecchia. *Dendritic cell traffic control by chemokines*, volume 1, pages 79–89. Birkhäuser Verlag, 2006.

[3] Samantha J Allen, Susan E Crown, and Tracy M Handel. Chemokine: receptor structure, interactions, and antagonism. *Annu Rev Immunol*, 25:787–820, 2007.

[4] Pablo A Iglesias and Peter N Devreotes. Navigating through models of chemotaxis. *Curr Opin Cell Biol*, 20(1):35–40, Feb 2008.

[5] Jason S King and Robert H Insall. Chemotaxis: finding the way forward with Dictyostelium. *Trends Cell Biol*, 19(10):523–30, Oct 2009.

Figure S1

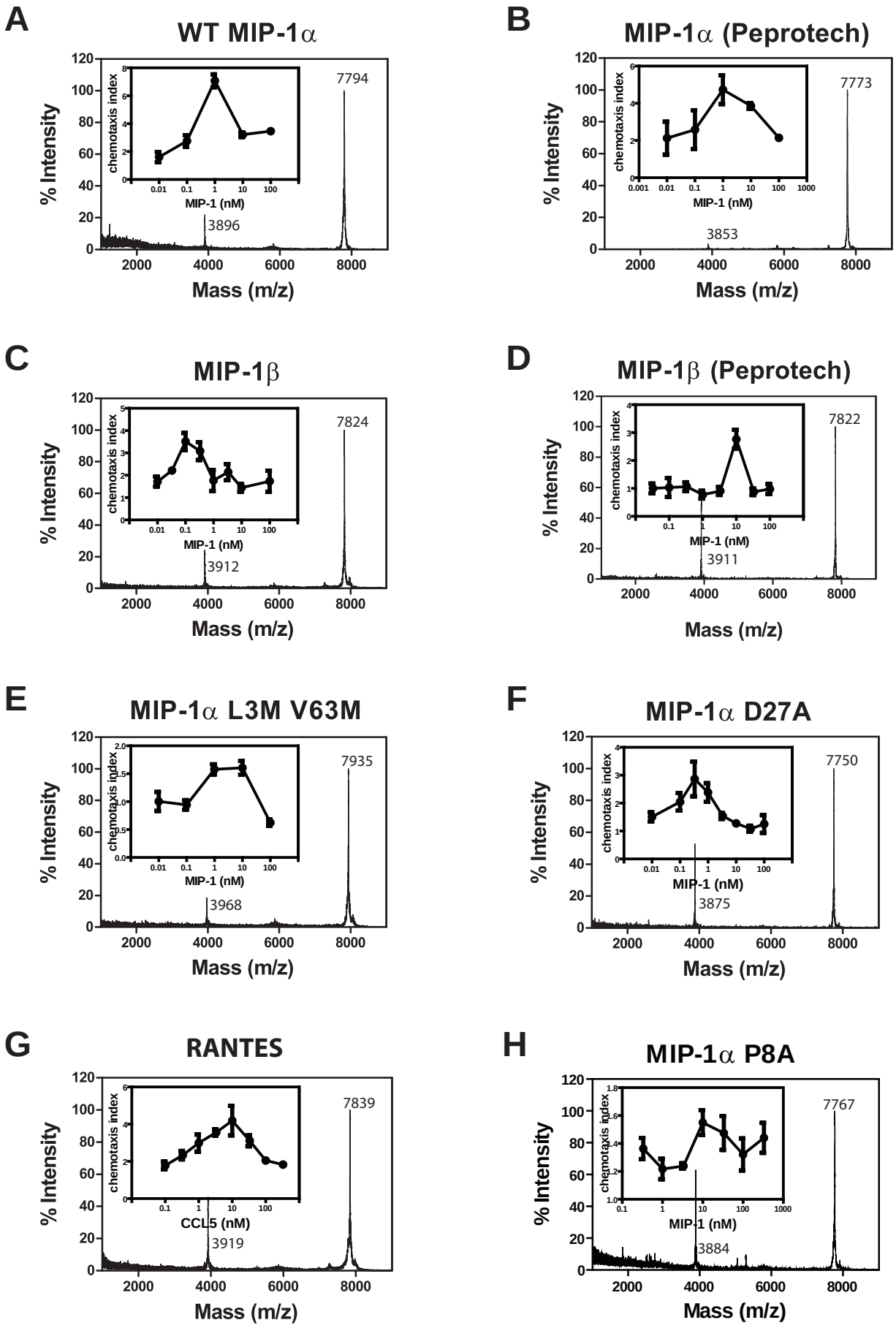
A
WT MIP-1α
7794
3896
B
MIP-1α (Peprotech)
7773
3853
C
MIP-1β
7824
3912
D
MIP-1β (Peprotech)
7822
3911
E
MIP-1α L3M V63M
7935
3968
F
MIP-1α D27A
7750
3875
G
RANTES
7839
3919
H
MIP-1α P8A
7767
3884
% Intensity
Mass (m/z)
chemotaxis index
MIP-1 (nM)
CCL5 (nM)

Figure S2

A

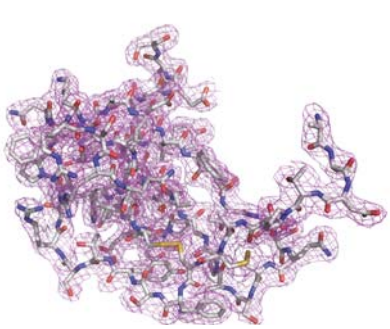

MIP-1α

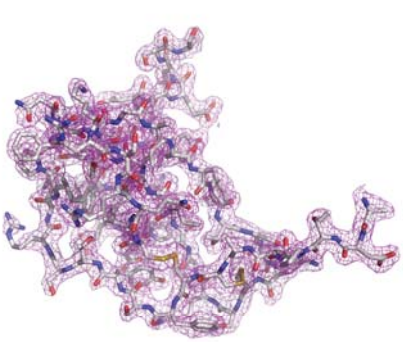

MIP-1α D27A

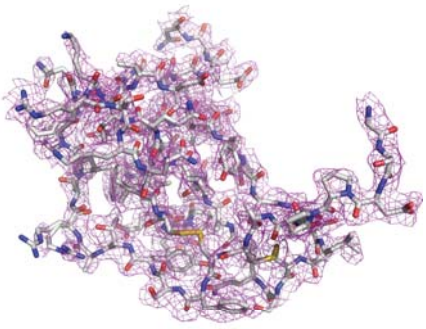

MIP-1β

B

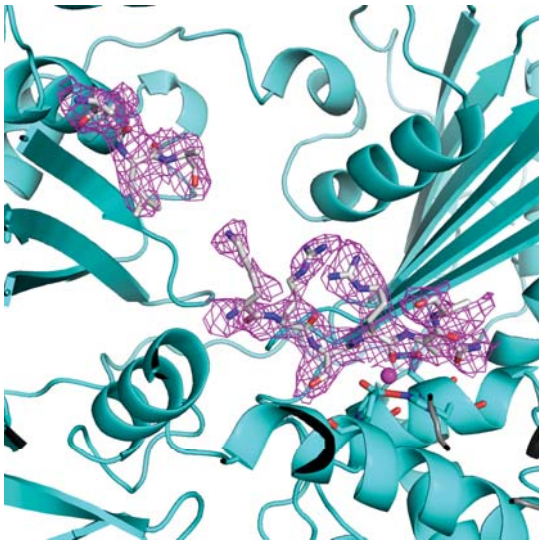

IDE/MIP-1α

Figure S3

A

MIP-1α (2x69) CCL1 (1EL0) CCL7(1BO0) CCL8(1ESR) CCL11(1EOT)

CCL13(2RA4) CCL15(2HCC) CCL23(1G91) CCL24(1EIG) CCL26(1G2S)

B

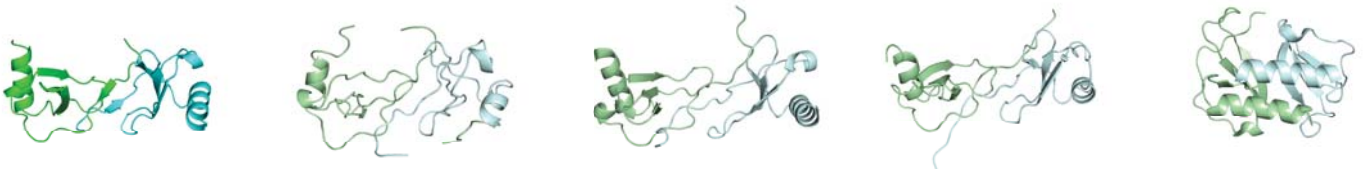

MIP-1α(2x69) MIP-1α(1B53) CCL4(1HUM) CCL5(1U4L) CCL20(2HCI)

C

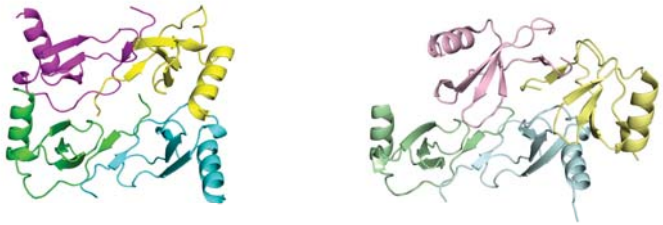

MIP-1α(2x69) CCL14(2Q8T)

Figure S4-1

A

Residue			Distance	Residue		
Intra layer (between A and B)						
A	SER	14[OG]	2.67	B	ASP	6[OD2]
A	CYS	51[N]	3.21	B	ASP	6[O]
A	CYS	11[N]	3.22	B	THR	9[O]
A	THR	9[N]	2.70	B	CYS	11[O]
A	CYS	11[O]	2.87	B	THR	9[N]
A	THR	9[O]	2.89	B	CYS	11[N]
A	ASP	6[OD2]	3.21	B	SER	14[OG]
A	ASP	6[OD1]	3.67	B	THR	16[OG1]
A	ASP	6[O]	3.20	B	CYS	51[N]
Crosslink (between A and D)						
A	SER	32[N]	3.59	D	ALA	5[O]
A	SER	32[OG]	3.69	D	ASP	6[OD2]
A	SER	33[N]	3.20	D	ASP	6[OD2]
A	ASP	6[OD2]	3.40	D	SER	32[OG]
A	ASP	6[OD1]	3.02	D	SER	33[N]
A	ASP	6[OD2]	3.41	D	SER	33[OG]
Interlayer(Between B and D)						
B	SER	17[OG]	3.79	D	SER	33[O]
B	ARG	18[NH1]	3.55	D	GLU	30[OE1]
B	ARG	46[N]	2.74	D	GLU	67[OE1]
B	ARG	46[NE]	2.87	D	ASP	27[OD1]
B	ARG	46[NH1]	2.92	D	LEU	66[O]
B	ARG	46[NH2]	3.69	D	ALA	26[O]
B	ARG	48[NH1]	3.85	D	GLU	30[OE2]
B	ARG	48[NH2]	3.19	D	TYR	28[OH]
B	TYR	15[O]	2.82	D	SER	33[OG]
B	ARG	18[NH1]	3.55	D	GLU	30[OE1]
B	ARG	46[NE]	2.87	D	ASP	27[OD1]
B	ARG	46[NH2]	3.49	D	ASP	27[OD1]
B	ARG	46[NH2]	3.98	D	ASP	27[OD2]
B	ARG	48[NH1]	3.85	D	GLU	30[OE2]

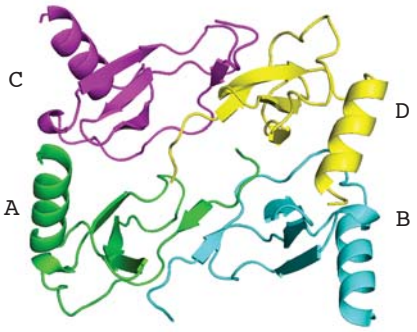

B

	Residue		ASA(Å²)	BSA(Å²)
B	SER	14	80.82	32.02
B	TYR	15	62.20	12.67
B	THR	16	40.89	8.14
B	SER	17	105.57	26.97
B	ARG	18	197.98	87.34
B	ASN	23	113.41	27.02
B	PHE	24	102.94	85.60
B	THR	44	17.96	11.66
B	LYS	45	141.14	39.21
B	ARG	46	193.14	124.97
B	ARG	48	145.30	84.39

	Residue		ASA(Å²)	BSA(Å²)
D	ALA	26	51.32	9.20
D	ASP	27	57.58	35.45
D	TYR	28	37.72	24.16
D	PHE	29	90.78	24.95
D	GLU	30	119.10	40.94
D	THR	31	16.49	0.25
D	SER	32	45.37	1.11
D	SER	33	118.81	71.42
D	GLN	34	156.14	25.30
D	PRO	38	92.73	25.27
D	GLY	39	1.60	0.29
D	PRO	54	32.43	22.18
D	SER	55	83.54	0.73
D	GLN	60	96.51	0.61
D	VAL	63	27.43	14.90
D	SER	64	43.34	15.73
D	LEU	66	55.26	30.83
D	GLU	67	104.99	104.37
D	LEU	68	150.12	58.39
D	SER	69	134.67	18.50

C

Monomer1	Monomer2	Interface(Å²)
A	B	678.2
A	D	286.5
B	D	533.4

Figure S4-2

A

Residue			Distance	Residue		
Intra layer (between A and B)						
A	SER	14[OG]	3.53	B	ASP	6[OD1]
A	CYS	51[N]	3.04	B	ASP	6[O]
A	CYS	11[N]	2.69	B	THR	9[O]
A	THR	9[N]	2.67	B	CYS	11[O]
A	CYS	11[O]	2.61	B	THR	9[N]
A	THR	9[O]	2.81	B	CYS	11[N]
A	ASP	6[OD1]	2.60	B	SER	14[OG]
A	ASP	6[O]	3.05	B	CYS	51[N]
Crosslink (between A and D)						
A	SER	5[N]	2.69	D	GLU	30[O]
A	SER	32[OG]	2.65	D	ASP	6[OD1]
A	SER	33[N]	3.41	D	ASP	5[O]
A	SER	34[N]	2.79	D	ASP	6[OD1]
A	ASP	5[O]	2.84	D	SER	33[N]
A	ASP	6[OD2]	2.86	D	SER	33[N]
A	ASP	6[OD1]	2.42	D	SER	33[OG]
Interlayer(Between B and D)						
B	LYS	45[N]	2.90	D	GLU	67[OE1]
B	ARG	46[N]	3.19	D	GLU	67[OE1]
B	ARG	48[NZ]	3.64	D	ASP	27[OD1]
B	ARG	48[NZ]	3.71	D	ASP	27[OD2]
B	TYR	15[O]	3.21	D	SER	33[OG]
B	ARG	46[NE]	3.99	D	ASP	27[OD1]
B	ARG	48[NZ]	3.64	D	ASP	27[OD1]
B	ARG	48[NZ]	3.71	D	TYR	27[OD2]

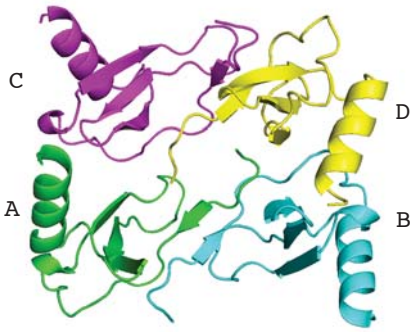

B

Residue			ASA(Å^2)	BSA(Å^2)
B	SER	14	81.14	41.77
B	TYR	15	67.29	10.44
B	THR	16	33.95	7.34
B	ALA	17	109.07	19.77
B	ARG	18	196.30	109.47
B	PRO	21	61.88	21.31
B	ASN	23	113.35	33.69
B	PHE	24	109.24	102.99
B	THR	44	13.13	7.70
B	LYS	45	137.78	42.52
B	ARG	46	179.35	79.95
B	ARG	48	120.98	66.23

Residue			ASA(Å^2)	BSA(Å^2)
D	VAL	26	71.40	2.09
D	ASP	27	68.21	32.85
D	TYR	28	46.32	33.43
D	TYR	29	88.16	10.87
D	GLU	30	99.73	22.80
D	THR	31	14.14	5.83
D	SER	32	37.97	1.85
D	SER	33	113.65	68.65
D	GLN	34	156.79	24.75
D	PRO	38	96.06	45.20
D	ALA	39	0.58	0.58
D	PRO	54	32.26	5.18
D	VAL	63	26.58	14.22
D	TYR	64	141.06	50.79
D	LEU	66	40.03	23.85
D	GLU	67	106.15	104.56
D	LEU	68	126.70	67.47
D	ASN	69	146.99	2.33

C

Monomer1	Monmer2	Interface(Å^2)
A	B	604.8
A	D	271.2
B	D	530.2

Figure S4-3

IDE Residue		Distance	MIP-1α Residue	
GLY	361[N]	3.11	ALA	1[O]
HIS	332[ND1]	3.82	SER	2[OG]
HIS	336[N]	3.40	SER	2[OG]
GLY	339[O]	2.94	ALA	1[N]
GLU	341[OE1]	2.63	ALA	1[N]
LEU	359[O]	3.10	ALA	1[N]
TYR	609[OH]	3.74	SER	2[N]
GLY	361[O]	3.17	LEU	3[N]
THR	220[OG1]	3.02	SER	18[OG]
THR	142[N]	2.99	SER	18[O]
GLN	111[NE2]	3.46	SER	18[O]
HIS	112[NE2]	2.80	ARG	19[O]
HIS	108[NE2]	3.53	ARG	19[O]
ASN	139[ND2]	2.63	GLN	20[O]
THR	142[O]	3.31	SER	18[N]
GLU	189[OE2]	2.81	ARG	19[N]
ALA	831[OH]	3.76	ALAL	21[N]

Figure S5

A

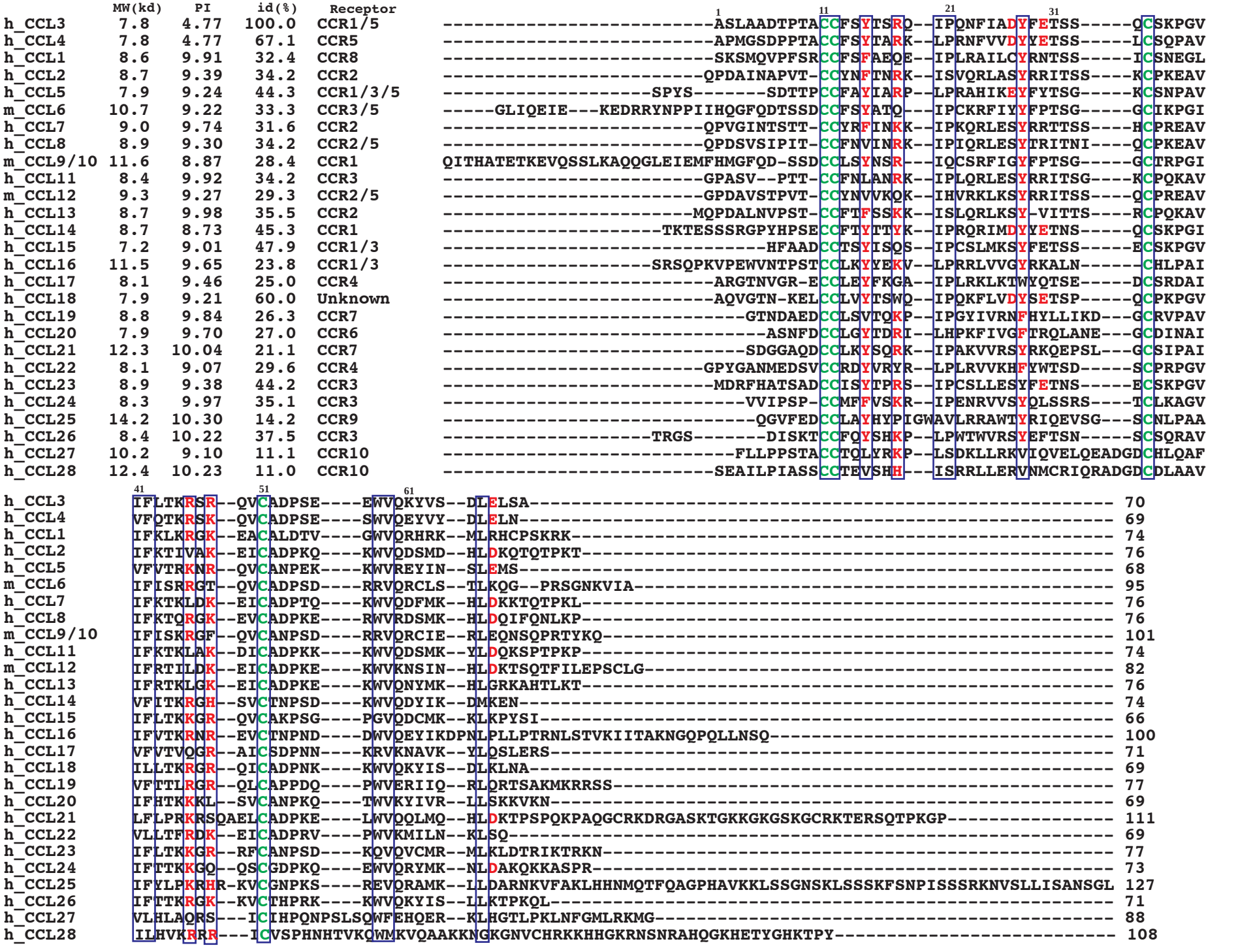
MW(kd) PI id(%) Receptor
h_CCL3 7.8 4.77 100.0 CCR1/5
h_CCL4 7.8 4.77 67.1 CCR5
h_CCL1 8.6 9.91 32.4 CCR8
h_CCL2 8.7 9.39 34.2 CCR2
h_CCL5 7.9 9.24 44.3 CCR1/3/5
m_CCL6 10.7 9.22 33.3 CCR3/5
h_CCL7 9.0 9.74 31.6 CCR2
h_CCL8 8.9 9.30 34.2 CCR2/5
m_CCL9/10 11.6 8.87 28.4 CCR1
h_CCL11 8.4 9.92 34.2 CCR3
m_CCL12 9.3 9.27 29.3 CCR2/5
h_CCL13 8.7 9.98 35.5 CCR2
h_CCL14 8.7 8.73 45.3 CCR1
h_CCL15 7.2 9.01 47.9 CCR1/3
h_CCL16 11.5 9.65 23.8 CCR1/3
h_CCL17 8.1 9.46 25.0 CCR4
h_CCL18 7.9 9.21 60.0 Unknown
h_CCL19 8.8 9.84 26.3 CCR7
h_CCL20 7.9 9.70 27.0 CCR6
h_CCL21 12.3 10.04 21.1 CCR7
h_CCL22 8.1 9.07 29.6 CCR4
h_CCL23 8.9 9.38 44.2 CCR3
h_CCL24 8.3 9.97 35.1 CCR3
h_CCL25 14.2 10.30 14.2 CCR9
h_CCL26 8.4 10.22 37.5 CCR3
h_CCL27 10.2 9.10 11.1 CCR10
h_CCL28 12.4 10.23 11.0 CCR10
1
11
21
31
41
51
61

B.

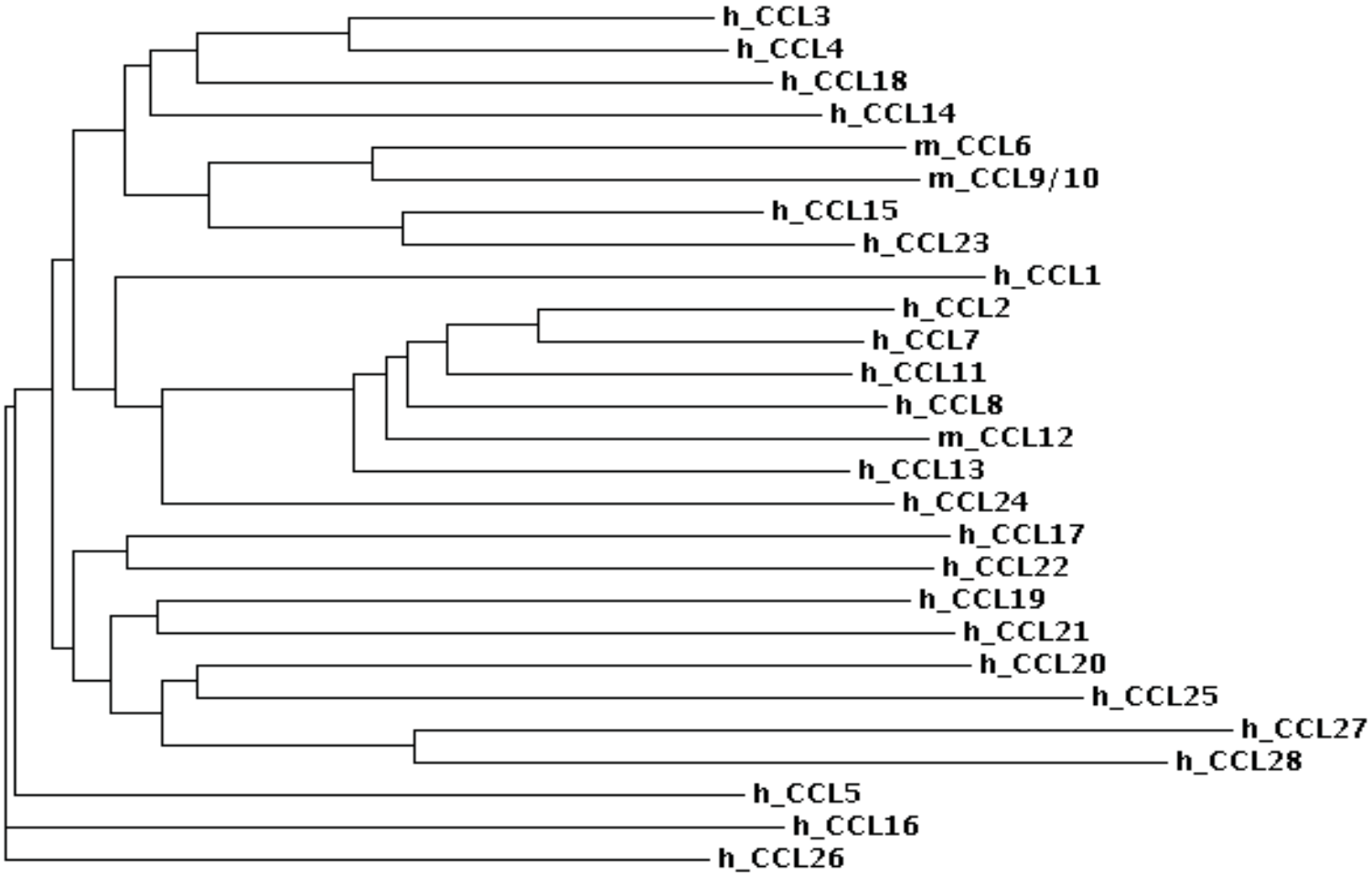
h_CCL3
h_CCL4
h_CCL18
h_CCL14
m_CCL6
m_CCL9/10
h_CCL15
h_CCL23
h_CCL1
h_CCL2
h_CCL7
h_CCL11
h_CCL8
m_CCL12
h_CCL13
h_CCL24
h_CCL17
h_CCL22
h_CCL19
h_CCL21
h_CCL20
h_CCL25
h_CCL27
h_CCL28
h_CCL5
h_CCL16
h_CCL26

Figure S6

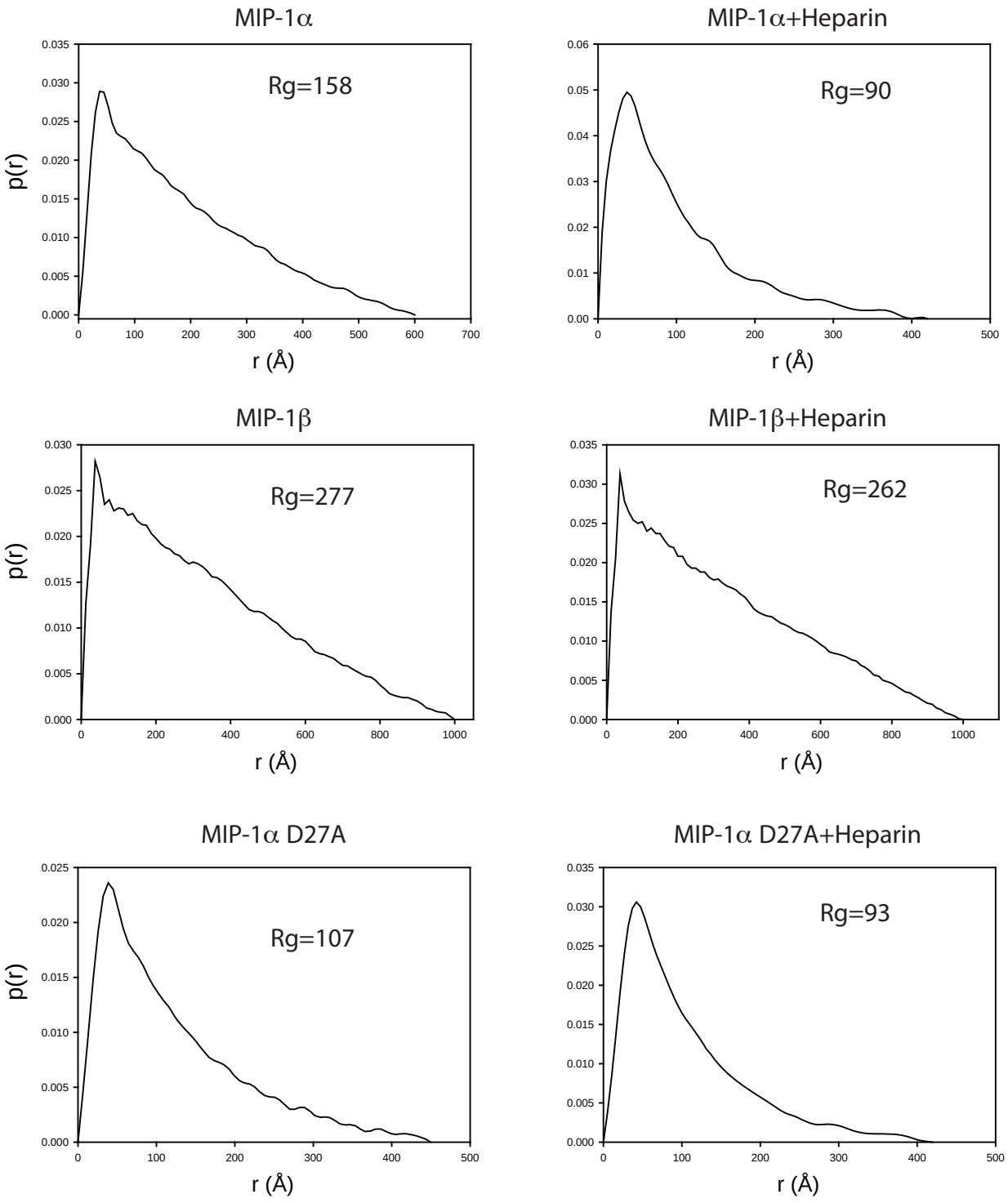
MIP-1α
Rg=158
MIP-1α+Heparin
Rg=90
MIP-1β
Rg=277
MIP-1β+Heparin
Rg=262
MIP-1α D27A
Rg=107
MIP-1α D27A+Heparin
Rg=93
p(r)
r (Å)

Figure S7

A

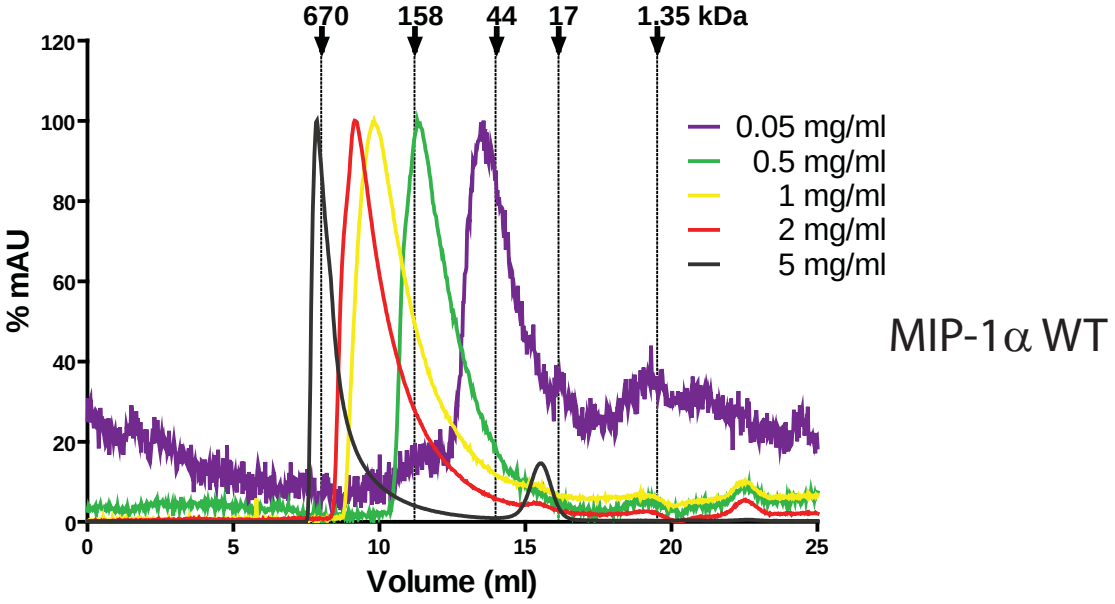

MIP-1α WT

B

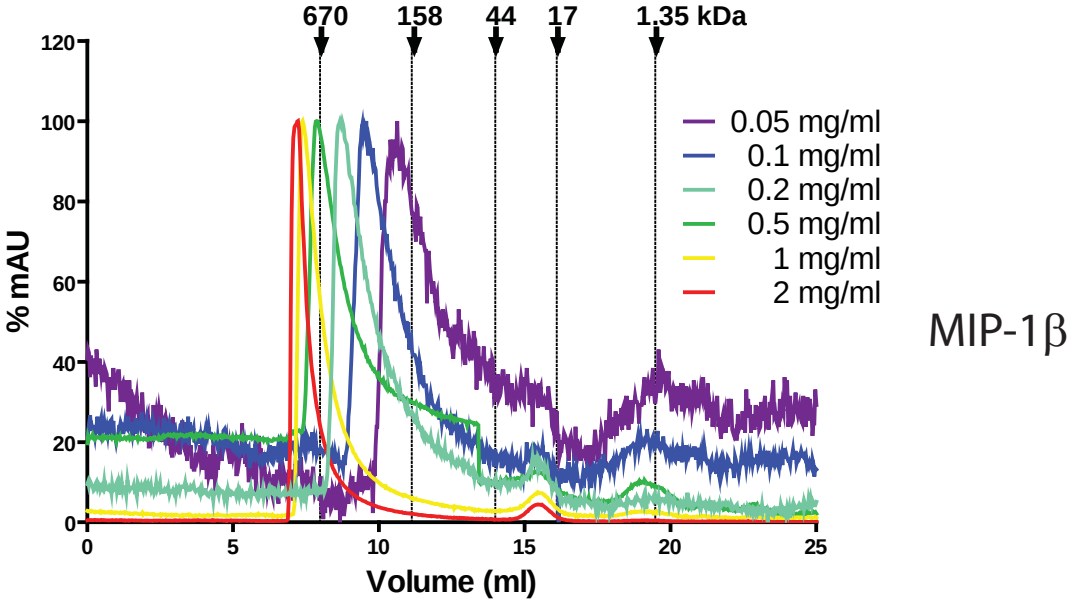

MIP-1β

C

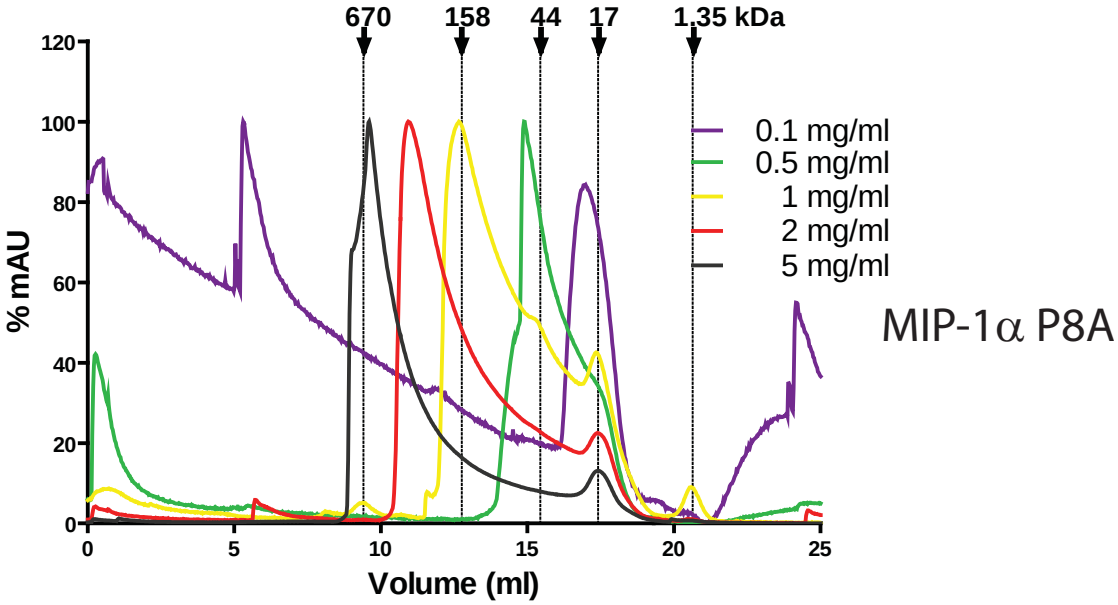

MIP-1α P8A

Figure S8

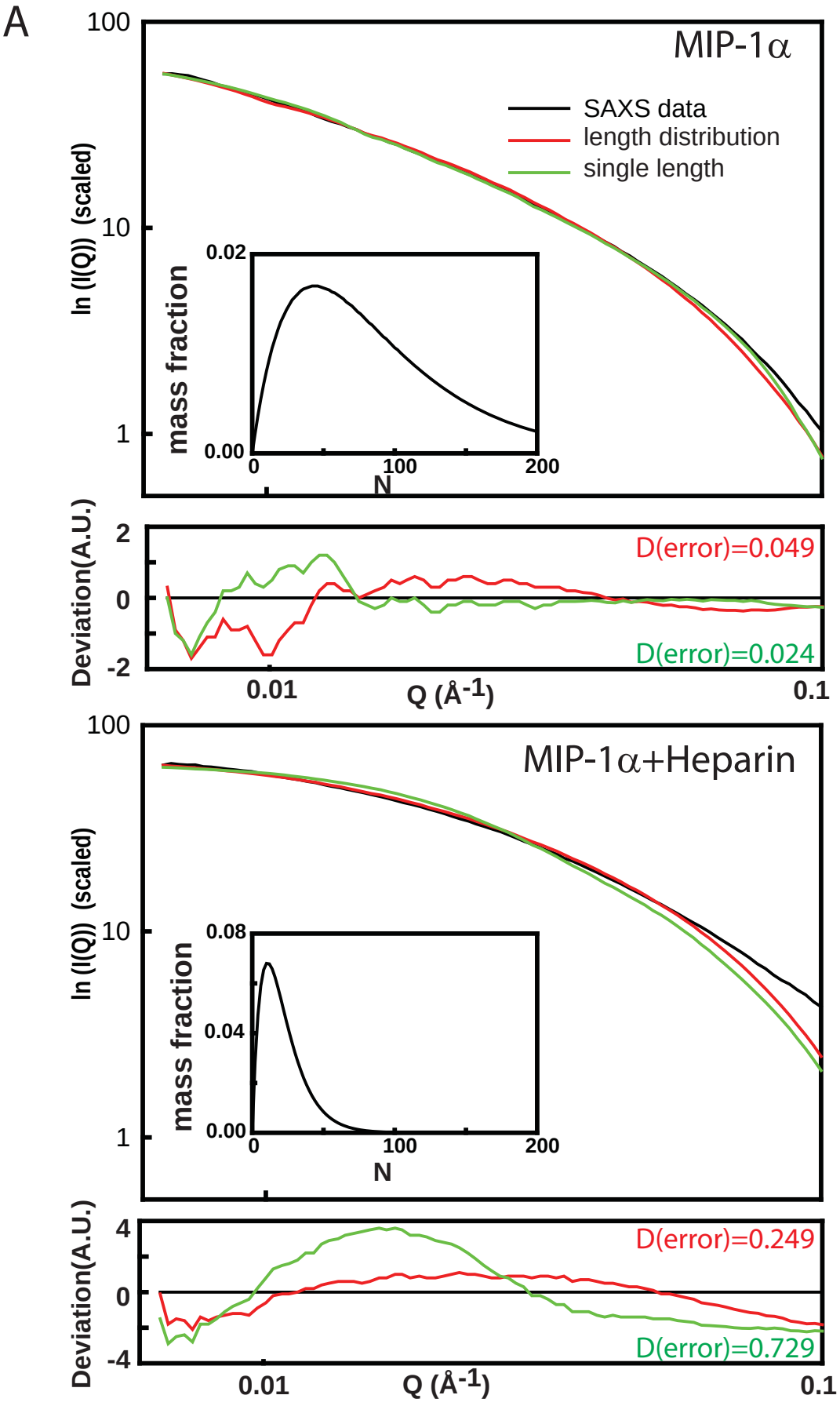
A
MIP-1α
SAXS data
length distribution
single length
ln (I(Q)) (scaled)
100
10
1
mass fraction
0.02
0.00
0
100
200
N
Deviation(A.U.)
2
0
-2
D(error)=0.049
D(error)=0.024
0.01
Q (Å-1)
0.1
MIP-1α+Heparin
0.08
0.04
4
-4
D(error)=0.249
D(error)=0.729

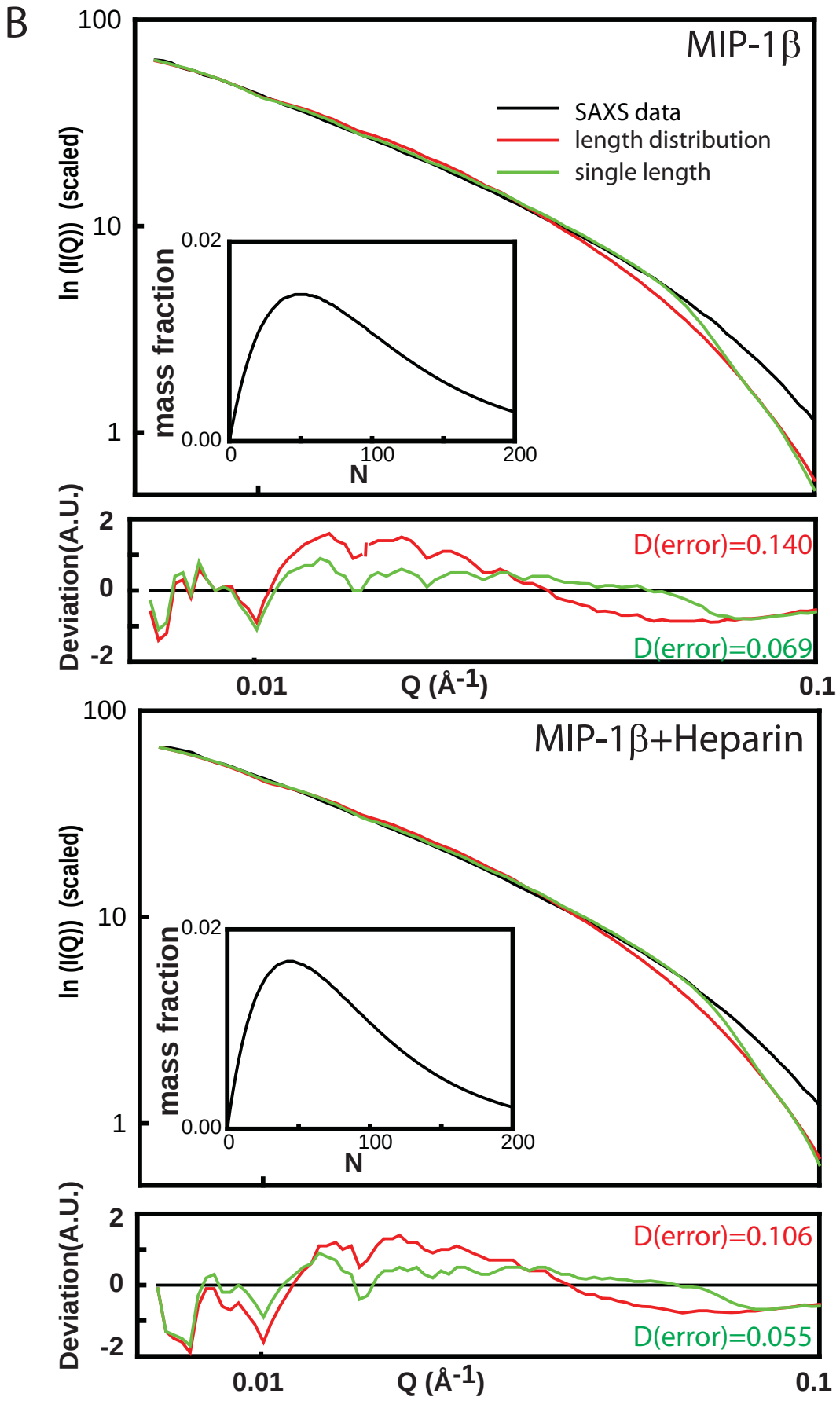
B
MIP-1β
SAXS data
length distribution
single length
ln (I(Q)) (scaled)
100
10
1
mass fraction
0.02
0.00
0
100
200
N
Deviation(A.U.)
2
0
-2
D(error)=0.140
D(error)=0.069
0.01
Q (Å-1)
0.1
MIP-1β+Heparin
D(error)=0.106
D(error)=0.055

C

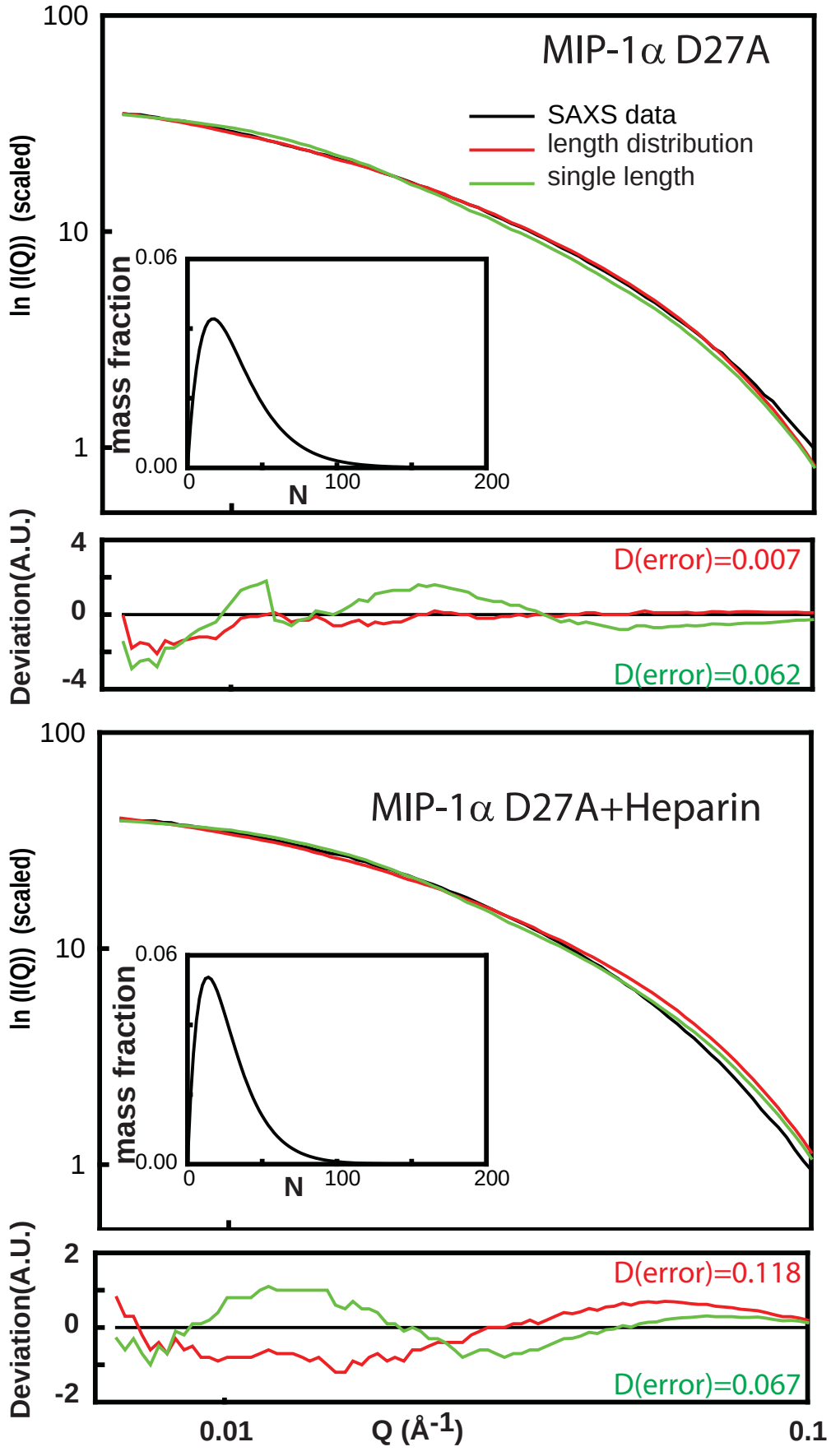
MIP-1α D27A
SAXS data
length distribution
single length
ln (I(Q)) (scaled)
100
10
1
mass fraction
0.06
0.00
0
100
200
N
Deviation(A.U.)
4
0
-4
D(error)=0.007
D(error)=0.062
MIP-1α D27A+Heparin
ln (I(Q)) (scaled)
100
10
1
mass fraction
0.06
0.00
0
100
200
N
Deviation(A.U.)
2
0
-2
D(error)=0.118
D(error)=0.067
0.01
Q (Å-1)
0.1

Figure S9

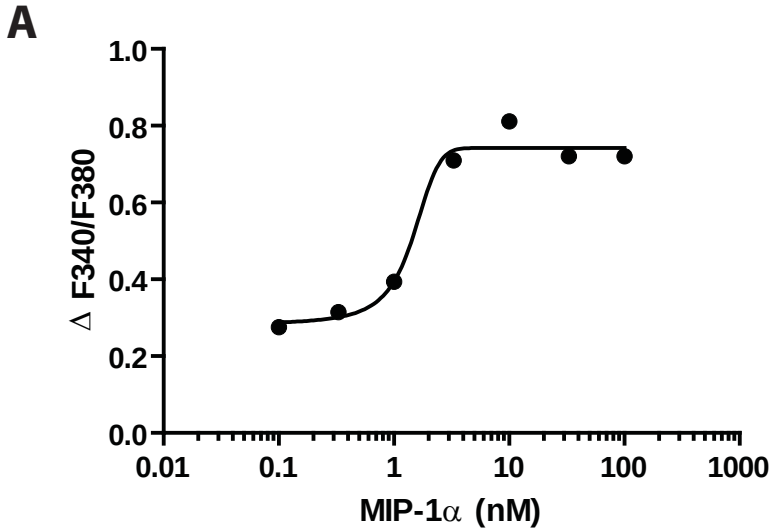
A
1.0
0.8
0.6
0.4
0.2
0.0
Δ F340/F380
0.01
0.1
1
10
100
1000
MIP-1α (nM)

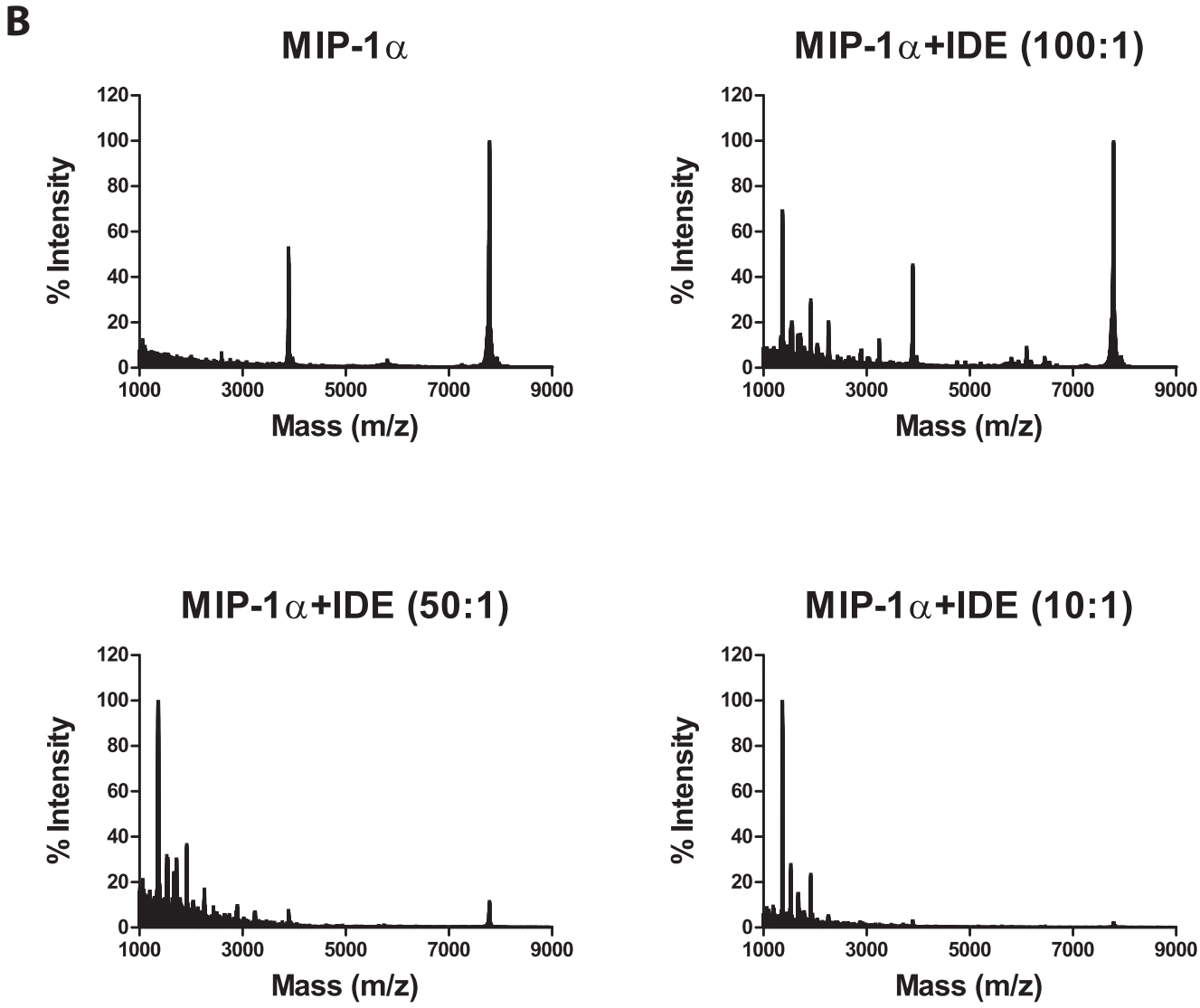
B
MIP-1α
MIP-1α+IDE (100:1)
MIP-1α+IDE (50:1)
MIP-1α+IDE (10:1)
% Intensity
Mass (m/z)
120
100
80
60
40
20
0
1000
3000
5000
7000
9000

Figure S10

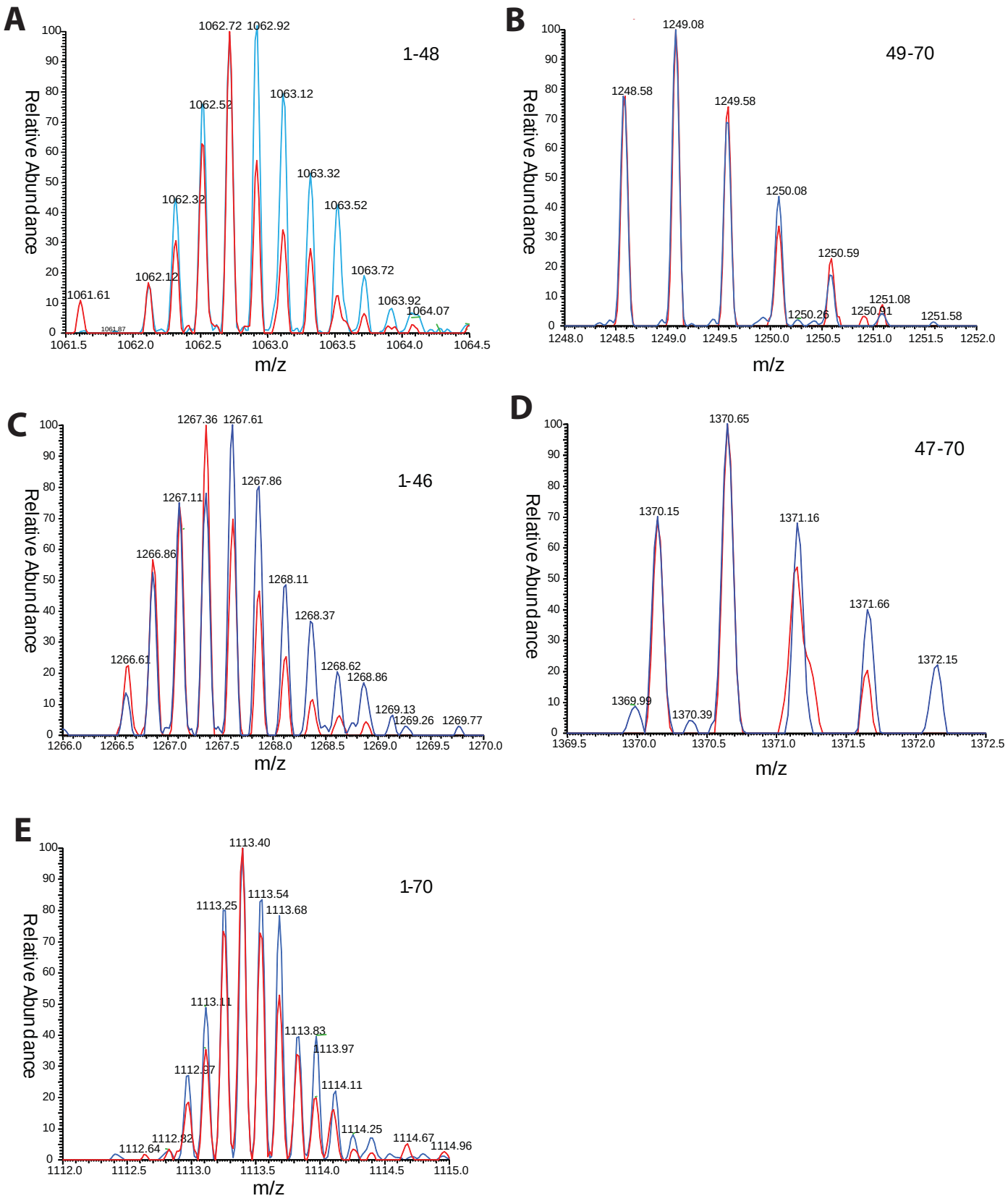
A
1-48
Relative Abundance
m/z
1062.72
1062.92
1062.52
1063.12
1062.32
1063.32
1063.52
1062.12
1063.72
1061.61
1063.92
1064.07
B
49-70
1249.08
1248.58
1249.58
1250.08
1250.59
1251.08
1250.26
1250.91
1251.58
C
1-46
1267.36
1267.61
1267.86
1267.11
1266.86
1268.11
1268.37
1266.61
1268.62
1268.86
1269.13
1269.26
1269.77
D
47-70
1370.65
1370.15
1371.16
1371.66
1372.15
1369.99
1370.39
E
1-70
1113.40
1113.54
1113.25
1113.68
1113.11
1113.83
1113.97
1112.97
1114.11
1114.25
1112.82
1114.67
1112.64
1114.96

Figure S11

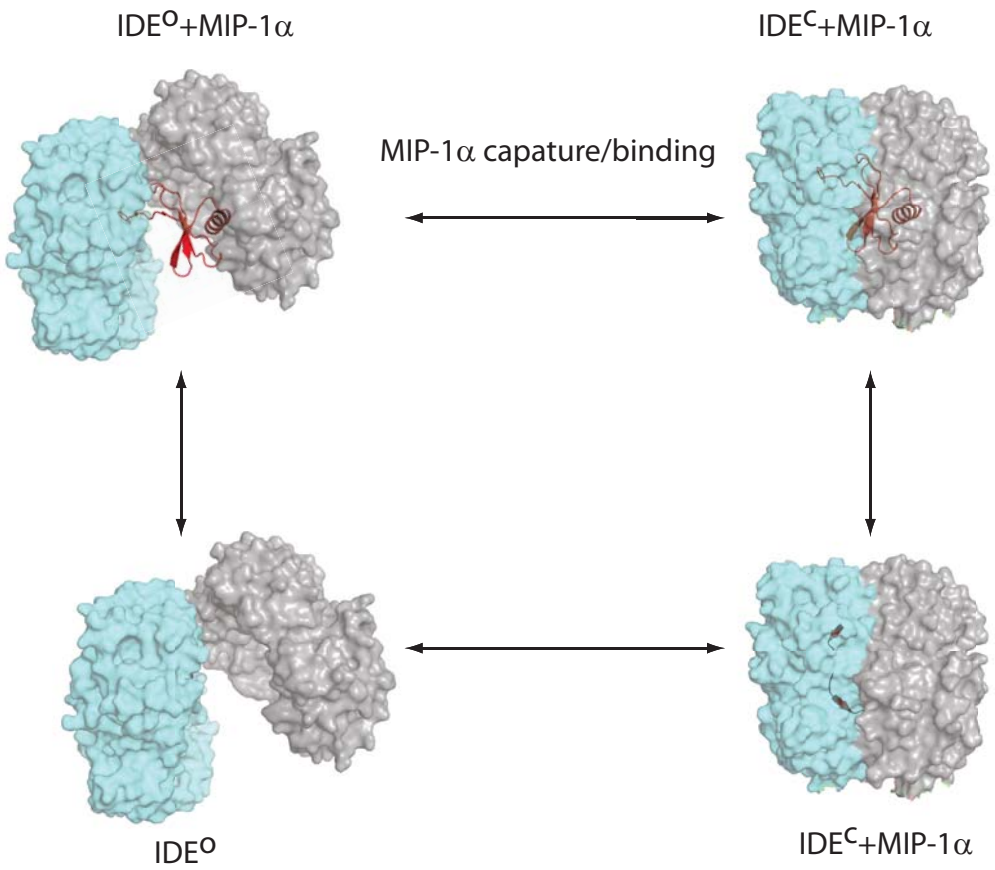
IDE^{O}+MIP-1α
IDE^{C}+MIP-1α
MIP-1α capature/binding
IDE^{O}
IDE^{C}+MIP-1α

Supplemental table 1: Crystallographic statistics of Se_MIP-1α (V3M/L63M)

Data collection			
	G7	G7	X53
Wavelength (Å)	0.97939(peak)	0.97953(inflection)	0.97939
Space group	C2	C2	C2
Cell dimension(Å)			
a	309.5	309.2	308.2
b	178.0	178.0	178.6
c	77.4	77.5	77.4
α	90	90	90
β	89.8	89.9	90.1
γ	90	90	90
Resolution (Å)	50-3.1	50-3.2	50-2.7
Rsym (%)[a]	12.6(59.2)[e]	13.4(57.5)	10.8(51.5)
I/sigma	29.3(3.2)[e]	25.8(3.9)	21.3(2.5)
Redundancy[b]	7.2(7.1)[e]	7.2(7.2)	3.6(3.7)
Completeness (%)	99.9(100.0)[e]	99.9(100.0)	99.8(100.0)
Unique reflections	78012	75739	113405
Figure of merit	0.874		
Refinement			
R_{work}[c]			0.204
R_{free}[d]			0.241
No. atoms			
Protein			15920
Water			385
B-factors			
Protein			38.2
Water			41.3
r.m.s. deviations			
Bond lengths (Å)			0.021
Bond angles (^{o})			1.949
Ramachandran plot (%)			
Favorable region			93.1
Allowed region			6.7
Generously allowed region			0.2
Disallowed region			0

[a] $R_{merge} = \Sigma\ (I - \langle I \rangle)/ \Sigma \langle I \rangle$

[b] N_{obs}/N_{unique}

[c] $R_{work} = \Sigma_{hkl}\ ||F_{obs}| - |F_{calc}||/ \Sigma_{hkl} |F_{obs}|$

[d] $\boldsymbol{R}_{free}$, calculated the same as for $\mathbf{R}_{work}$ but on the 5% data excluded from the refinement calculation.

[e] the outer resolution shell. Values in parentheses indicate the highest resolution shell

Supplemental Table-2

	MIP-1α	MIP-1α +Heparin	MIP-1α D27A	MIP-1α D27A +Heparin	MIP-1β	MIP-1β +Heparin
Radius of Gyration (Å)						
R_g (Guinier)[1]	130	80	100	80	150	140
R_g (p (r))[2]	160	90	100	90	280	260
R_c[3]	17	15	17	19	17	17
Width (Å)						
Diameter[4]	49	42	49	55	47	47
Length (Å)						
R_c+R_g(Guinier)[5]	430	270	330	280	510	490
R_c+R_g(p(r))	540	310	370	320	960	910
D_{max} (Å)	600	420	450	420	950[6]	950[6]
Subunits in polymer						
SEC	90	70	4	20	230	200
R_c+R_g(Guinier)[7]	40	25	30	25	46	44
R_c+R_g(p(r))[7]	50	30	30	30	90	80
Length distribution[8]	60	22	34	28	100	88
Single length[8]	50	24	34	28	72	64
Kd(nM)[9]						
Length distribution[8]	290	2130	890	1310	100	130

[1] The value of the radius of gyration (R_g) was derived from the Guinier approximation: $I(q) = I(0) \exp(-q^2R_g^2/3)$, in the q-range $qR_g < 1.3$, where $I(q)$ is the scattered intensity and $I(0)$ is the forward scattered intensity

[2] The Radius of gyration (R_g) defined by P(r) was calculated by using the following formula:

$$R_g^2 = \int_0^{D_{max}} r^2 P(r) dr \Big/ \int_0^{D_{max}} P(r) dr$$

[3] The value of the radius of gyration (R_c) was derived from the Guinier approximation: $q*I(q) \sim q*I(0) \exp(-q^2R_c^2/2)$, in the medium q-range, where $I(q)$ is the scattered intensity and $I(0)$ is the forward scattered intensity.

[4] Diameter of the cross-section was calculated by using the following equation: $D=2*2^{1/2}*R_C$

[5]Length (L) was calculated by using the following equation $L=(12*(R_g^2-R_C^2))^{1/2}$

[6]listed D_{max} were maximal value based on the measurement limits of the experiment and generated by software GNOM

[7]Subunits in polymer was calculated by following calculation: N=L/22*2 while 22Å is the distance between two dimers.

[8] Curve fitting use theoretical SAXS scattering

[9] Dissociation constant corresponding to the breaking of a dimer-dimer bond. In accord with Eqs. (14) and (20) of the Supplemental Mathematical Modeling, this constant is calculated as $K_d = \frac{8c_t}{d^2 - 4}$, where c_t is the initial MIP monomer concentration and d, the average degree of polymerization, is determined from the "length distribution" fit to the SAXS data.

Table S3 Summary of mass spectrometry analysis of MIP1α fragments resulting from IDE initial cleavage.

FRAGMENT	CAL MASS (M+H)	OBS MASS (M+H) (LC-FT-ICR)	Δppm	MS/MS (b/y ions)	O18 labeling
1-70	7783.713	7783.677	4.57		no[a]
1-45	4907.336	4907.321	3.07	b5-7, b16, b19; y5, y11	yes
46-70	2895.394	2895.388	1.94	b7-8, b^{++}6-8, b^{++}11-23; y10, y17, y^{++}9, y^{++}14-16, y^{++}18, y^{++}21, y^{++}24-25	no
1-46	5063.438	5063.424	2.77	b4-b7, b12-15; y4-5, y7, y9-11, y14	yes[a]
47-70	2739.293	2739.288	1.68	b5-b16; y10-y15, y17	no[a]
1-48	5306.571	5306.557	2.65	b4-8, b11; y5, y10, y12,	yes[a]
49-70	2496.160	2496.153	2.74	b5, b8-10, b12-17; y7-10, y12-14, y17	no[a]
1-18	1864.820	1864.814	3.18	b4-13, b15; y3-15	yes
19-70	5937.910	5937.907	0.47	b8-9; , b^{++}12, b^{++}18-21, b^{++}25, b^{++}35; y7-13, y17, y^{++}13-14, y^{++}17-20, y^{++}22, y^{++}28, y^{++}25	no

Summary of mass spectrometry analysis of MIP-1α fragments resulting from IDE initial cleavage. Calculated and observed masses are shown as singly charged monoisotopic mass (M+H). Observed b/y ions according to the specific fragment from tandem mass spectrometry analysis are listed. MIP-1α was digested with IDE in 50% ^{18}O water. The fragments labeled with ^{18}O are marked as "yes" in the last column. [a]Example spectrums of ^{18}O labeling experiment were shown in Fig. S10.

Table S4 Summary of mass spectrometry analysis of IDE degraded MIP1α fragments .

FRAGMENT	CAL MASS (M+H)	OBS MASS (M+H) (LC-FT-ICR)	OBS MASS (M+H) (MALDI-TOF)	Δppm
4-18	1593.667	1593.660	N/D	4.83
5-18	1522.630	1522.620	N/D	6.63
6-18	1451.5929	1451.597	N/D	2.83
8-18	1235.518	1235.516	N/D	1.79
8-46	4434.136	4434.126	N/D	2.11
21-46	2976.492	2976.476	N/D	5.68
25-46	2490.250	2490.306	N/D	22.69
26-46	2377.186	2377.182	N/D	1.40
27-46	2306.149	2306.153	N/D	1.78
30-46	1880.990	1880.979	N/D	5.95
31-46	1751.947	1751.945	N/D	1.26
26-48	2620.319	2620.310	N/D	3.39
17-28	1451.728	N/D	1451.724	2.55
18-28	1364.696	N/D	1364.693	1.97
14-24	1340.659	N/D	1340.661	1.26
1-13	1270.544	N/D	1270.720	138.52
15-27	1552.775	N/D	1552.762	8.63